

Spatio-temporal evolution of the $L \rightarrow I \rightarrow H$ transition

K. Miki,¹ P. H. Diamond,^{1,2,3} Ö. D. Gürçan,⁴ G. R. Tynan,² T. Estrada,⁵ L. Schmitz,⁶ and G. S. Xu⁷

¹WCI Center for Fusion Theory, National Fusion Research Institute, Daejeon 305-333, South Korea

²Center for Momentum Transport and Flow Organization, University of California, San Diego, California 92093, USA

³Center for Astrophysics and Space Science, University of California, San Diego, California 92093, USA

⁴LPP, Ecole Polytechnique, CNRS, France

⁵Laboratorio Nacional de Fusión, Asociación Euratom-CIEMAT, Madrid, Spain

⁶University of California, Los Angeles, California 90095, USA

⁷Institute of Plasma Physics, Chinese Academy of Science, Hefei, China

(Received 10 July 2012; accepted 4 September 2012; published online 19 September 2012)

We investigate the dynamics of the low(L) \rightarrow high(H) transition using a time-dependent, one dimensional (in radius) model which self-consistently describes the time evolution of zonal flows (ZFs), mean flows (MFs), poloidal spin-up, and density and pressure profiles. The model represents the physics of ZF and MF competition, turbulence suppression via $E \times B$ shearing, and poloidal flows driven by turbulence. Numerical solutions of this model show that the $L \rightarrow H$ transition can occur via an intermediate phase (I-phase) which involves oscillations of profiles due to ZF and MF competition. The I-phase appears as a nonlinear transition wave originating at the edge boundary and propagates inward. Locally, I-phase exhibits the characteristics of a limit-cycle oscillation. All these observations are consistent with recent experimental results. We examine the trigger of the $L \rightarrow H$ transition, by defining a ratio of the rate of energy transfer from the turbulence to the zonal flow to the rate of energy input into the turbulence. When the ratio exceeds order unity, ZF shear gains energy, and a net decay of the turbulence is possible, thus triggering the $L \rightarrow H$ transition. Numerical calculations indicate that the $L \rightarrow H$ transition is triggered by this peak of the normalized ZF shearing. Zonal flows act as “reservoir,” in which to store increasing fluctuation energy without increasing transport, thus allowing the mean flow shear to increase and lock in the transition. A counterpart of the $L \rightarrow I \rightarrow H$ transition, i.e., an $L \rightarrow H$ transition without I-phase, is obtained in a fast power ramp, for which I-phase is compressed into a single burst of ZF, which triggers the transition. Effects of neutral charge exchange on the $L \rightarrow H$ transition are studied by varying ZF damping and neoclassical viscosity. Results show that the predicted $L \rightarrow H$ transition power increases when either ZF damping or viscosity increase, suggesting a link between recycling, ZF damping, and the $L \rightarrow H$ threshold. Studies of fueling effects on the transition and pedestal structure with an emphasis on the particle pinch are reported. © 2012 American Institute of Physics. [<http://dx.doi.org/10.1063/1.4753931>]

I. INTRODUCTION

Understanding of $L \rightarrow H$ transition physics is crucial to a successful ITER. The $L \rightarrow H$ transition to a state of the higher confinement was discovered at ASDEX.¹ Understanding of the power requirement for accessing the H-mode is so essential that intensive experimental surveys of threshold power in various physical parameters have been carried out.^{2,3} The power threshold tends to have different behavior in lower and higher density regions. However, a successful theoretical framework within which to understand the physics of the $L \rightarrow H$ transition and a theoretical prediction of the threshold power have not yet been realized, due to uncertainty concerning the trigger of the transition. The trigger of the transition has not been specified yet. To determine the threshold power scalings, a physical understanding of the trigger is necessary.

In experiments, prior to the $L \rightarrow H$ transition, as power slowly increases, several kHz quasi-periodic evolution of the E_r (radial electric field) was first observed in ASDEX-

Upgrade, and referred to as a dithering cycle.⁴ Instead, with a fast heat power ramp rate, only a few such cycles appear, while with a slow ramp rate, or at steady power, an extended series of limit-cycle oscillations is observed. This quasi-periodic behavior prior to the $L \rightarrow H$ transition is also seen in JET,⁵ DIII-D,⁶ etc.

Theoretically, the $L \rightarrow H$ transition is regarded as a transport bifurcation, which is related to $E \times B$ flow shear suppression by multiple types of flows: zonal flow (ZF) and mean flow (MF).⁷ Here, mean $E \times B$ flow (MF) $\langle V_E \rangle$ is generated mainly by diamagnetic flow due to global pressure and density profiles, while zonal flow V_{ZF} is fluctuation driven and has a mesoscale radial structure. The mesoscale spectral range is $\Delta_c < l_{\text{meso}} < L_p$, where $\Delta_c \sim \rho_i$ is the turbulence correlation length and L_p is a system size characterized by pressure scale length. The mesoscale range may be typified by the geometric mean of the micro and macro scales,⁸ $l_{\text{meso}} \sim \sqrt{\Delta_c L_p}$. However, we emphasize that “mesoscale” refers to a range of the scales and not a single scale! Therefore, ZF and MF shearing should be distinguished.

Shear enhanced decorrelation of turbulent fluctuations has been proposed as a mechanism for confinement improvement and turbulence suppression.^{9,10} A mean field predator-prey model originally describes the interplay between turbulence fluctuation and the diamagnetic-driven $E \times B$ mean flow, exhibiting self-consistency, i.e., the turbulence fluctuation and the mean flow amplitude are closely related to, and are determined by, one another.¹¹ Reference 12 extended the self-consistent predator-prey system, coupling turbulence with the ZF, using the conservation of the wave action with the flow shear.

Reference 13 proposed a predator-prey model describing interacting ZF and MF shear suppression of turbulence, a simplified coupling of the mean flow shear and pressure gradient by radial force balance, and MF-ZF competition. The model recovers an L-H transition triggered by ZF shearing and a pre-transition limit-cycle oscillation (LCO) due to interplay among turbulence, ZF, and MF. The interplay occurs on a slow zonal flow damping time scale and manifests a phase delay between turbulence and shearings. Here, this model study finds that ZF shearing is an important ingredient in the L \rightarrow H transition, because ZF mediates the transition, reduces turbulence level, enhances MF evolution, and thus regulates the power threshold. When the importance of the ZF to transition was noticed, it was realized that since zonal flow is fluctuation driven, ZF can trigger the transition but cannot sustain it. Thus, the transition intrinsically must be a *two predator* (ZF and MF) and one prey problem. Mean flow shear affects the fluctuation-driven Reynolds correlation, as well as fluctuation intensities. In this two predator-one prey model, the zonal flow triggers the transition, while the mean flow “locks in” to the H-mode state.

TJ-II has identified the physical mechanism behind the L \rightarrow H transition from the limit-cycle oscillation of E_r interacting with turbulent fluctuations.¹⁴ The experimental results clearly show limit-cycles in the E_r and turbulence fluctuations in phase space, suggesting a strong similarity to the model of Ref. 13. Other experimental devices also have studied the pre-transition limit-cycle oscillation, which is referred as to intermediate (I)-phase in NSTX, ASDEX-Upgrade, DIII-D, and EAST.^{15–18}

Note that a dynamical system analysis of the model of Ref. 13 indicates that the LCO occurs around a saddle (structurally unstable) fixed point, referred as to the transient state.¹⁹ This should be distinguished from L \rightarrow H \rightarrow L periodic transition, as is previously discussed in Ref. 4. This is because the transient state LCO is defined by the feedback loop of turbulence and ZF shearing, and thus the ZF damping determines the time scale of the oscillation.

With regard to the pre-transition LCO, spatio-temporal structure of this sort has now been identified in DIII-D¹⁷ and TJ-II.²⁰ A Doppler backscattering system (DBS) has measured local density fluctuation and total $E \times B$ flow, with high spatial and temporal resolution.¹⁷ This measurement has provided a new picture of the I-phase as an evolving flow layer structure of LCO. The LCO structure resembles a propagating wave. Density fluctuations are peaked outside of the separatrix and are reduced across separatrix in an around 2–3 cm wide layer. Via alternative methodology, propagating

structure has been also elucidated by simultaneous measurement at two radial locations, with a two-channel Doppler reflectometer in TJ-II.²⁰ This study identified two-way propagation of E_r oscillations depending on the measured line density, i.e., some cases of lower line density $(2 - 25) \times 10^{19} \text{ m}^{-3}$ show outward propagation, and some particular cases of higher line density $3 \times 10^{19} \text{ m}^{-3}$ exhibit inward propagation. The outward propagation speed is the largest at the innermost radial position and gradually decreases as the oscillation reaches the edge E_r shear position. This phenomenon may be linked to the radial spreading of the turbulence from the plasma core to the edge barrier.²¹

To relate these findings to the two predator-one prey hypothesis of ZF trigger and mediation, at least a one space dimension version of the multi-predator-prey model¹³ is necessary here. Such a one-dimensional model can predict the *spatio-temporal* evolution of the pedestal through the L \rightarrow H transition, as well as the spatial structure of the LCO in I-phase. Note that since no “first principles” simulation has ever successfully recovered the L \rightarrow H transition, reduced models are the only option. Also, in the event that useful “first principles” simulations become available in the future, reduced models will still be necessary to extract the essence of the transition physics—i.e., to distill the lesson learned.

In this paper, we present novel theoretical results on the spatio-temporal dynamics of L \rightarrow H transition, with special emphasis on the role of ZFs in the trigger process. We present comparison to several recent experimental results. We extend the earlier transition models¹³ to develop a 5-field reduced mesoscale model which evolves turbulence intensity, zonal flow shear, pressure and density profiles, and mean poloidal mass flow in *both* radius and time. The mean $E \times B$ velocity shear $\langle V_E \rangle'$ is calculated via radial force balance using density and pressure profiles and poloidal flow. We present evidence that the ZF can trigger the transition.

To support the hypothesis that the ZF is fundamental to the transition, we explore the sensitivity of the L \rightarrow H threshold to the ZF damping. As ZF shearing can trigger the L \rightarrow H transition and downshift the power threshold, larger ZF damping should weaken the ZF shearing and turbulence suppression and *upshift* the power threshold. Higher ZF damping can result from higher neutral charge exchange (CX). An increase of the neutral CX friction can be caused by wall saturation, increased re-cycling, etc., leading to increased ZF damping and increased neoclassical poloidal flow viscosity. This damping acts in addition to that originating from ion-ion collisions. This indicates that the wall physics and recycling can alter the L \rightarrow H power threshold and that high edge neutral density is unfavorable to transition.²² Based on this hypothesis, we examine how ZF mediates the L \rightarrow H transition in higher neutral CX cases.

We also study how the early stages of pedestal formation depend upon particle fueling. As particle fueling originates at the edge boundary, a particle pinch effect must be considered, so as to allow build-up of the density profile. However, the effects of the particle pinch on L \rightarrow I \rightarrow H transition and pedestal formation have not been discussed. Related to the particle pinch, the deposition layer width is another comparable factor. The deposition layer width is

really set by the fueling method, i.e., pellet injection or gas puffing. Thus, we here investigate two issues regarding fueling: (i) how the particle pinch affects L \rightarrow H transition dynamics and (ii) how the fueling deposition width affects the pedestal structure.

The remainder of this paper is organized as follows. In Sec. I, we introduce the reduced 5-field mesoscale model, the related physics, and the initial conditions and parameters. In Sec. II, we present basic numerical results of the L \rightarrow H transition and comparison to experimental results. In Sec. III, we discuss numerical results regarding the power threshold study and pedestal profiles. Here, we also suggest implications for experiments based on the results. In Sec. IV, we conclude and discuss remaining issues.

II. STRUCTURE OF THE MODEL

To better understand L \rightarrow I \rightarrow H transition dynamics, we propose a theoretical model as an extension of the two predator-one prey system¹³ to treat dynamics and evolution in the radial dimension r . The model describes space-time evolutions of turbulence intensity (I), zonal flow shear energy ($E_0 = V_{ZF}^{\prime 2}$), pressure (p) and density (n) profiles, and mean poloidal mass flow ($\langle v_\theta \rangle$). These quantities are averaged over fine scales and fast times. Thus, *a priori*, the spatial scale is longer than ρ_i and the evolution scale is slower than drift wave time $\omega_*^{-1} \sim (c_s/a)^{-1}$, in order to satisfy the scale separation requirement for wave kinetics, which is the foundation of our reduced model.⁷ The basis is the following predator-prey model with one prey (turbulence intensity) and two predators (ZF and MF shearings):

$$\partial_t I = I(\gamma_L - \Delta\omega I - \alpha_0 E_0 - \alpha_V E_V) + \chi_N \partial_r(I \partial_r I), \quad (1)$$

$$\partial_t E_0 = \frac{\alpha_0 E_0 I}{1 + \zeta_0 E_V} - \gamma_{\text{damp}} E_0. \quad (2)$$

Here, we assume that turbulence originates from the ion channel; the first term on the r.h.s. of Eq. (1) represents turbulence generation by ion temperature gradient (ITG) mode via linear instability, where $\gamma_L = \gamma_{L0}(c_s/R)\sqrt{(R/L_T) - (R/L_T)_{\text{crit}}}$ is the local growth rate of turbulence intensity, with a critical temperature gradient parameter $(R/L_T)_{\text{crit}}$, $c_s = \sqrt{T_{i0}/m_i}$ is the ion sound speed, T_{i0} is a reference ion temperature, m_i is the ion mass, R and a are major and minor radii, respectively, and $L_T = |d \ln T / dr|^{-1}$ is the scale length of the ion temperature gradient. The temperature profile is calculated from $T = p/n$. The model is flexibly adaptable to other instabilities, by changing the definition of γ_L , to that for the trapped electron modes, etc. The second term on the r.h.s. of Eq. (1) represents the nonlinear damping by self-saturation of turbulence due to local spectrum broadening, the increment parameter for which is given by $\Delta\omega$. The third and fourth terms represent turbulence suppression due to ZF and MF shearing, respectively. There $\alpha_0 \sim \tau_{ac}$ is a shearing coupling coefficient proportional to the auto-correlation time between turbulence and zonal flow group propagation,^{11,23} and α_V is the shearing coupling coefficient between turbulence and MF shear. The detailed derivation of the shearing

coupling parameters is discussed in Appendix A. The fifth term of the r.h.s. of Eq. (1) represents the nonlocal turbulence spreading,²¹ where the turbulent thermal diffusivity is $\chi_N \sim \chi_{N0}(\rho_* c_s^2/a)$, and we assume turbulence spreading is diffusive with $D \sim \chi_N \sim D_{\text{GB}}$.²⁴

The first term on the r.h.s. of Eq. (2) represents turbulent Reynolds drive, with enhancement of decorrelation of drift wave propagation by a MF shear, which enters the cross phase in the Reynolds stress. ζ_0 represents the inhibition of zonal flow growth by MF shear due to weakening of the response of drift wave spectrum to a seed ZF.¹³ The derivation of the effect on ZF shearing by MF shear is summarized in Appendix B. The second term on the r.h.s. of Eq. (2) represents damping of ZF shear, where γ_{damp} is the ZF damping rate originating from ion-ion collisionality and also neutral CX. $\gamma_{\text{damp}} = \gamma_{\text{damp},0} \nu_{ii}/R$ and $\gamma_{\text{damp},0} = 1 + \nu_{\text{CX}}/\nu_{ii}$, where ν_{ii} is the ion-ion collision frequency and ν_{CX} is neutral CX friction. Here, we neglect the dependence of the neutral CX friction on the density profile, for simplicity. The sensitivity of ZF damping to ion collisionality has been elucidated by direct numerical simulation (DNS) using the gyrokinetic equation, e.g., see Ref. 25. $E_V = \langle V_E \rangle^2$ is MF shear energy. The MF shear is obtained from the radial force balance equation. To separate the evolution of mean flow from that of zonal flow, we assume that pressure and density profiles should evolve on time scale much slower than zonal flows. This is due to the fact that ZF is distributed throughout the *mesoscale* spectrum (i.e., $l \sim \sqrt{\Delta_c L_p}$, $\tau \sim \sqrt{\Delta_c L_p}/c_s < L_p/c_s$), while MF are macroscale (i.e., $l \sim L_p$).

We obtain γ_L and E_V from the global profiles, p and n . The evolution of the pressure and density profiles are given by the following one-dimensional transport equations with external sources:

$$\partial_t p + (1/r) \partial_r(r \Gamma_p) = \partial_r H, \quad (3)$$

$$\partial_t n + (1/r) \partial_r(r \Gamma_n) = \partial_r S. \quad (4)$$

Here, H and S are the external heat and particle source flux profiles, respectively, given by

$$\partial_r H = Q_a \exp\left(-\frac{r^2}{2L_{h,\text{dep}}^2}\right), \quad (5)$$

$$\partial_r S = \Gamma_a \frac{a-r+d_a}{L_{\text{dep}}^2} \exp\left[-\frac{(a-r+d_a)^2}{2L_{\text{dep}}^2}\right], \quad (6)$$

for which typical profiles are illustrated in Fig. 1. Note that source is flux-driven both for particles and heat. The heat flux H is located in the core with the amplitude Q_a , while the particle flux S is fueled in the edge region with amplitude Γ_a , the deposition width L_{dep} , and the shift of a gaussian peak from the edge, d_a .

Γ_n and Γ_p are given by the following equations, consisting of diffusive and convective (pinch) terms:

$$\Gamma_n = -(D_{\text{n.t.}} + D_0) \partial_r n + V_n n, \quad (7)$$

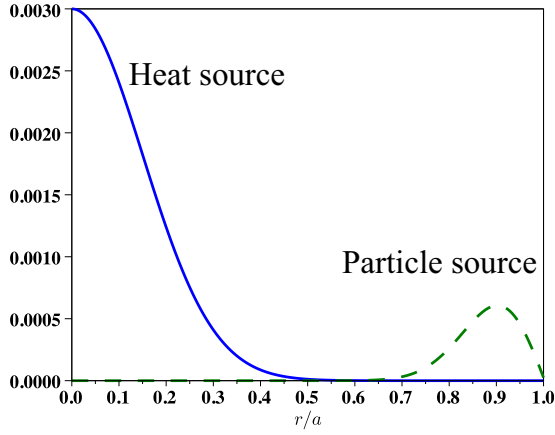


FIG. 1. Profiles of heat (solid) $\partial_r H$ and particle (dotted) $\partial_r S$ sources in the case with $L_{h,dep}/a = 0.15$, $d_a/a = 0.0$, $L_{dep}/a = 0.10$, and arbitrary Q_a and Γ_a . The heat source is localized in the core. The particle source is localized at the edge with a given, fixed deposition width.

$$\Gamma_p = -(\chi_{n.t.} + \chi_0) \partial_r p. \quad (8)$$

Here, $D_{n.t.}$ and $\chi_{n.t.}$ are non-turbulent particle and heat diffusivities in H-mode, respectively, corresponding to the neoclassical transport. D_0 and χ_0 correspond to turbulent particle and thermal diffusivities of the electrostatic turbulence, respectively given by

$$D_0 = \chi_0 = \frac{\tau_c c_s^2 I}{1 + \alpha_t \langle V_E \rangle^2}. \quad (9)$$

Note that τ_c is the correlation time of turbulence and α_t is a cross-phase modification by mean flow, normalizing the MF shear $\langle V_E \rangle^2$. Here, we assume the particle and the heat fluxes have the same basic correlation time scale, i.e., we neglect possible differences in cross-phases of the diffusivities, for simplicity. The mean flow shear suppression factor α_t also appears in Refs. 24, 26, and 9. As low β is assumed, there is no magnetohydrodynamics (MHD) activity—edge localized modes (ELMs), etc., *after* the development of the pedestal. Describing such evolution is beyond the scope of this paper. We thus consider only electrostatic turbulence here.

V_n is the particle pinch velocity,²⁷ given by

$$V_n = -V_{n0} (D_{n.t.} + D_0) \left(\frac{2}{R} + \frac{1}{L_T} \right), \quad (10)$$

where the first term of the latter set of parenthesis on the RHS of Eq. (10) represents a turbulent equipartition (TEP) pinch²⁸ and the second term is a thermodiffusive pinch.^{29,30} Note that both pinch velocities are inward for ITG turbulence. Note also the total particle flux could be negative, at least transiently, until the density gradient steepens in H-mode. This is because a large heat flux can drive a strong inward density pinch via the ITG mode. The particle pinch consists of the TEP and thermodiffusive pinch, $V_n = V_{TEP} + V_{Th}$. The thermodiffusive pinch is proportional to the turbulence intensity, as given by $V_{Th} \propto -|\phi|^2 |\nabla T|$. Since $|\nabla T| \sim Q/\chi$ follows, where Q is the heat flux and χ is the local heat diffusivity, we have $V_{Th} \sim Q$. Thus, $\Gamma_n < 0$ is

possible if sufficient heat flux is carried. This has been observed, i.e., probe studies of particle flux show cross phase of V_r and n such that total flux is inward.³¹ Note that this observation applies to the H-mode pedestal and not to the L-mode preceding the transition. Of course, the particle pinch causes density profile peaking, so roughly $\nabla n/n \sim V/D$. We do not include a heat pinch in the pressure evolution, because the heat source is assumed to be applied in the core, and we are not concerned with global temperature profile structure.

By coupling toroidal and parallel force balance equations, we obtain the time evolution of poloidal mass flow,³²

$$-\frac{\partial \langle v_\theta \rangle}{\partial t} = \frac{B}{nm_i} \langle \nabla \cdot (\hat{e}_\theta \overleftrightarrow{\Pi}_{\text{turb}}) \rangle + B \mu^{(\text{neo})} (\langle v_\theta \rangle - \langle v_\theta^{(\text{neo})} \rangle), \quad (11)$$

where B is a toroidal magnetic field. The first term in the r.h.s. represents poloidal spin-up driven by turbulence through the stress tensor, which may be replaced with radial divergence of the Reynolds stress through the Taylor identity. $\mu^{(\text{neo})} = \mu_0^{(\text{neo})} \nu_{ii} [q(r)]^2 R^2$ is the neoclassical poloidal viscosity, $q(r)$ is the safety factor, $\mu_0^{(\text{neo})} = \mu_{00} (1 + \nu_{CX}/\nu_{ii})$, and μ_{00} is calculated from the energy weighted momentum equation.³³ Here, we assume the neutral CX friction can be added to the ion-ion collisionality in the neoclassical poloidal viscosity $\mu^{(\text{neo})}$, as well as the ZF damping. $\langle v_\theta^{(\text{neo})} \rangle = -(\mu_{01}/\mu_{00}) L(\psi) B_\theta \simeq -1.17 \nabla T$, given by Ref. 33, is the neoclassical poloidal flow velocity. Assuming slab geometry and constant B , we simplify Eq. (11) to

$$\frac{\partial \langle v_\theta \rangle}{\partial t} = -\alpha_5 \frac{\gamma_L}{\omega_*} c_s^2 \frac{\partial I}{\partial x} - \mu_0^{(\text{neo})} \nu_{ii} q^2 R^2 \left(\langle v_\theta \rangle - 1.17 c_s \frac{\rho_i}{L_T} \right), \quad (12)$$

We here use γ_L denoted in Ref. 32. This is the same as used in Eq. (1) of this model and $\omega_* \sim c_s/L_n \sim c_s/a$ is fixed. Note that the contribution from the zonal flow shearing to the Reynolds drive is neglected here, due to the scale separation assumption.

The $E \times B$ mean flow shear $\langle V_E \rangle'$ is related to the density and pressure gradients, the second derivative of the pressure profile, and the mean poloidal mass flow $\langle v_\theta \rangle$ by the radial force balance equation,

$$\langle V_E \rangle' = \frac{1}{eB} \left[-\frac{n'p'}{n^2} + \frac{p''}{n} \right] + a \left(\left\langle \frac{v_{\parallel}}{qR} \right\rangle' - \langle v_\theta \rangle' \right), \quad (13)$$

which can be rewritten as

$$\langle V_E \rangle' = \rho_i c_s L_p^{-1} (-L_n^{-1} + L_p^{-1}) - \langle v_\theta \rangle', \quad (14)$$

where $L_f = (d \ln f / dr)^{-1}$ for $f = n, p, p'$. Here, the first term in Eq. (13) corresponds to diamagnetic shearing, proportional to pressure and density gradient. The second term is the pressure profile curvature, proportional to the second derivative of pressure profile. The pressure profile curvature is often dropped because of difficulty in the analyses (e.g., Ref. 26), but some references discuss effects of the pressure

profile curvature on the transition.^{34,35} The profile curvature term becomes important especially when there is a corner in the profile. At the top of the pedestal in the H-mode profile, there necessarily must be a corner, and thus the profile curvature is large. How the pressure curvature evolves through L \rightarrow H transition is not yet clear. Therefore, we here keep this term and investigate its evolution. The fourth term corresponds to a contribution from the mean poloidal momentum. Here, we neglect the toroidal momentum of the third term in Eq. (13), for simplicity. This effect likely is essential for internal transport barrier (ITB) formation, however.³⁶

Note that this model can be reduced to the local predator-prey model of Ref. 13 with the following simplification. In Eqs. (1) and (2), neglecting the nonlocal effect ($\chi_N = 0$), and letting $\gamma_L = \mathcal{N}$, where $\mathcal{N} \propto (-dp/dr)$, we obtain the evolution equations for turbulence intensity and zonal flow shearing. These correspond to Eqs. (6) and (7) in Ref. 13. Using the simplified radial force balance of Eq. (14), assuming a constant temperature profile, neglecting the second derivative and toroidal and poloidal momentum, we obtain $\langle V_E \rangle' = d\mathcal{N}^2$. Reference 13 described the evolution of \mathcal{N} by the expression $\partial_t \mathcal{N} = Q - (c_1 + c_2 I) \mathcal{N}$ in Eq. (3). There Q is the heat source and c_1 and c_2 are the collisional/residual and turbulent transport coefficients, respectively.

A. Parameters and boundary conditions

Finally, we obtain the 5-field ($I, E_0, p, n, \langle v_\theta \rangle$) equations (Eqs. (1)–(4) and (12)) and the radial force balance equation, Eq. (13). We numerically solve these equations, using a finite difference method in radial space, and an implicit method of lines for the time integration, with the following conditions and parameters.

The simulation region is a cylindrical, one-dimensional space between $r=0$ at core and $r=a$ at the edge. Boundary conditions are the following, simplest set. For pressure and density profiles, we take

$$\begin{aligned} p(r=a) &= 0.01, & n(r=a) &= 0.1, \\ p'(r=0) &= n'(r=0) = 0, \\ p'''(r=0, a) &= n'''(r=0, a) = 0. \end{aligned}$$

Here, p and n are normalized by the reference quantities $n_0 = 10^{20} [\text{m}^{-3}]$ and $p_0 = T_{i0} n_0 = 1 [\text{keV}] \times 10^{20} [\text{m}^{-3}]$, respectively. We apply free boundaries at the cores of p and n but fixed boundaries at the edge. For the second derivatives of p and n at the edge, we impose the free boundary conditions, thus the third derivatives are also set to zero. We assume no interaction between the edge and scrape-off-layer (SOL) region and use a simple boundary condition. We believe that the free-forced boundary condition on the second derivative is the simplest applicable one. The simple boundary condition is consistent with experimental results, since quantities at the last closed flux surface (LCFS) are mostly constant during the L \rightarrow H transition in experiments. Here, we neglect any explicit modeling of SOL region ($r > a$). If we go beyond the free boundary condition, a sep-

aratrix SOL-edge model is necessary to match to. This is beyond the scope of this paper and will be addressed in future work.

Note that we need to deal with the poloidal asymmetry and X-point structure in a complete model. This requires modelling of the SOL flows and the effect of the edge boundary condition. In the present model, we simply assume a simulation box inside the LCFS and a fixed boundary at the edge. We present further discussion of this issue in Sec. IV. The study of detailed models will be pursued in the future.

For turbulence intensity, ZF, and mean poloidal flow, we impose

$$\begin{aligned} I'(r=0) &= I'(r=a) = E'_0(r=0) = E'_0(r=a) \\ &= \langle v_\theta \rangle'(r=0) = \langle v_\theta \rangle'(r=a) = 0. \end{aligned}$$

The other parameters we used in this numerical simulation are the following: The amplitude of particle flux source Γ_a is held constant at $\Gamma_a = 10^{-4}$. The strength of heat flux power Q_a ramps linearly from 1.0×10^{-4} to 3.2×10^{-2} , after reaching initial equilibrium from arbitrary initial conditions. Here, Γ_a and Q_a are normalized by $(c_s n_0)$ and $(c_s p_0)$, respectively.

The ion-ion collision frequency, ν_{ii} ,³⁷ normalized by the ion cyclotron frequency $\omega_{ci} = eB/m_i$, is

$$\frac{\nu_{ii}}{\omega_{ci}} = \frac{n_0 Z^4 e^4 \ln \Lambda}{3^{1/2} 6\pi \epsilon_0^2 m_i^{1/2} T_{i0}^{3/2}} \left(\frac{eB}{m_i} \right)^{-1}. \quad (15)$$

Here, we assume a single hydrogen ion, $Z=1$, $A=1$, $e = 1.6 \times 10^{-19} [\text{C}]$, $\Lambda = 20$, $B = 3.5 [\text{T}]$, $m_i = 1.67 \times 10^{-27} [\text{kg}]$, ϵ_0 is the dielectric constant of vacuum, and $T_{i0} = 1 [\text{keV}]$ is a reference ion temperature.

For the non-turbulent particle and thermal diffusivities in H-mode, we use the following thermal diffusion coefficients in the banana region:

$$\chi_{Ti} = \epsilon_t^{-3/2} [q(r)]^2 \rho_i^2 \nu_{ii}, \quad (16)$$

$$D_{ie} \sim (m_e/m_i)^{1/2} \chi_{Ti}, \quad (17)$$

where m_e is the electron mass. We set the safety factor (q) profile, $q(r) = 0.95 + 2.0 \times (r/a)^2$. Here, the transport in H-mode should be related to the neoclassical transport, (χ_{Ti} and D_{ie} , respectively), and other residual turbulence transport in H-mode. To model the non-turbulent transport, we apply the enhancement parameters $\chi_{n.t.} = 30\chi_{Ti}$ and $D_{n.t.} = 15\chi_{Ti}$, for the purpose of numerical convenience. With only ITG turbulence, we could not obtain proper initial profiles from the time evolution in the arbitrary initial condition, in the case with lower or purely neoclassical χ_{Ti} and D_{ie} . To obtain correct initial equilibria, some modest residual particle diffusion is necessary to control the density gradient. The actual residual particle transport in the pedestal is not yet understood and remains a topic of active research. This set of the parameters still retains the necessary qualitative properties, since $\chi_{n.t.} > D_{n.t.}$, $\chi_0 \gg \chi_{n.t.}$, and $D_0 \gg D_{n.t.}$ are satisfied.

Here, we apply a digital filter to the 5-field evolutions in each time step for the purpose of smoothing or compensating irrelevant higher radial wavenumber oscillations.^{38,39} The digital filter can correspond to hyper-viscosities in the field evolutions, which determine a minimum scale size of the mesoscale profile structure. The scale is determined by finite Larmor radius effects or neoclassical polarization shielding, based on gyrokinetic theory. We here avoid a specified estimation of the hyper-viscosities, but retain the essence of the model by using a digital filter with an arbitrary resolution. We set the digital filter so as to maintain the long wavelength radial structure $\Delta \gtrsim \rho_i$ and to effectively dissipate the short wavelength structure $\Delta \lesssim \rho_i$. This treatment also ensures the radial scale separation law of the mesoscale envelope from the turbulence scales.

Other parameters are $\rho_* = (\rho_i/a) = 0.01$, $\epsilon_t = a/R = 0.25$, $L_{h,dep}/a = 0.15$, $L_{dep}/a = 0.10$, $d_a/a = 0$, $\tau_c = 1.0(a/c_s)$, $\alpha_t = 1.0(a/c_s)^2$, $\gamma_L = \Delta\omega = 10^{-2}(c_s/R)$, $\alpha_0 = 1.0 \times 10^2 \sqrt{\rho_*}$ (c_s/a), $\alpha_V = 2.0 \times 10^{-2} \sqrt{\rho_*}(c_s/a)$, $\zeta_0 = 10^2(a/c_s)^2$, $(R/L_T)_{crit} = 3.7$, $\gamma_{damp} = 1.0\nu_{ii}/R(c_s/a)$, $\chi_N = 0.5\rho_*(a/c_s)^2$, $\mu_{00} = 1.0a^{-2}$, $\alpha_5 = 5.0 \times 10^3$, and $V_{n0} = 1.0$. Radial space and time scales are normalized by the minor radius a and the characteristic time of the drift wave $\omega_*^{-1} = (a/c_s)$, respectively. The radial grid size is $\Delta r/a = 1/400$, and the time step is $\Delta t(c_s/a) = 0.125 - 0.5$.

III. BASIC STUDIES OF L \rightarrow I \rightarrow H TRANSITION DYNAMICS

With the parameters described above, in Fig. 2, we present a numerical result which shows an L \rightarrow I \rightarrow H transition using a slow power ramp. As can be seen clearly, there are three distinct stages. The early stage, L-mode, is identified as a state with slowly growing turbulence, self-regulated by zonal flows. In the L-mode, as MF shearing is weak, the inter-

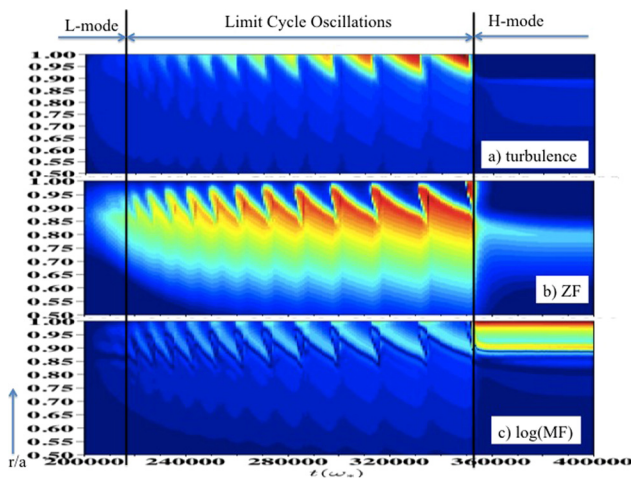


FIG. 2. Spatio-temporal evolution of turbulence intensity I , (a) (b) ZF shearing energy E_0 , and (c) logarithm of MF shearing energy $\ln(E_V)$ as functions of time t during a power ramp ($2 \times 10^5 < t < 4 \times 10^5$) and as a function of radius ($0.5 < r/a < 1.0$). Three distinct stages, L-mode, I-phase (LCO), and H-mode, are evident. In L-mode, turbulence and ZF grow self-consistently from the edge region; In I-phase, extended space and time structure of turbulence intensity, ZF, and MF appears. At the transition, turbulence and ZF drop rapidly. After transition, decay of turbulence and ZF is seen, while mean shear persists.

action between ZF and MF shearing is not significant, i.e., little decorrelation of ZF shearing by MF shear appears (see also Fig. 10(c)). As the heat flux through the edge increases with power, the system evolves into the next stage, namely the I-phase. The I-phase, which starts at $t = 2.16 \times 10^5(a/c_s)$, is characterized by the presence of nonlinear shearing waves, nucleated near the edge boundary and propagating inward while also expanding outward. The nonlinear shearing wave structure is consistent with that observed in DIII-D.¹⁷ Local phase portrait of the nonlinear waves appears with the LCOs observed in other experiments. These are triggered by an increase of ZF in the edge region ($0.90 < r/a < 1.00$). One example of the local phase portrait is shown in Fig. 3, plotting ZF energy E_0 and MF shear energy E_V in I-phase ($t = 2.4 - 3.2 \times 10^5(a/c_s)$) at the edge region, $r/a = 0.975$. The plots show quasi-periodic behavior with a certain phase relation. During the I-phase, a radially coherent phase shift among local values of turbulence, ZF, and MF can be identified. Once the ZF shear increases, the MF follows the behavior of the ZF shear. At $t = 3.53 \times 10^5(a/c_s)$, the L \rightarrow H transition occurs. At the transition, the I-phase terminates abruptly with the quench of the edge turbulence on a fast time scale and that of ZF in a slower time scale. The time scale that ZF decreases after the transition corresponds to the ZF damping rate. On the other hand, some weak turbulence and ZF persist on the pedestal shoulder, even after the transition. Note that here, the actual transition time scale is very short, even for a slow power ramp! During the transition, the pedestal begins to expand inward, as the MF shear grows rapidly. The transition time is a mixture of turbulence transport and neoclassical transport time scales.⁴⁰ Crudely, it is estimated as ~ 1 msec for DIII-D parameters. After the L \rightarrow H transition, the pedestal width still expands slowly inward and then saturates at $\Delta_{ped} \sim 0.10a$ in $t > 3.6 \times 10^5(a/c_s)$.

Fig. 4 shows a bird's-eye view of the space-time evolutions of turbulence intensity, ZF, and MF for the same case

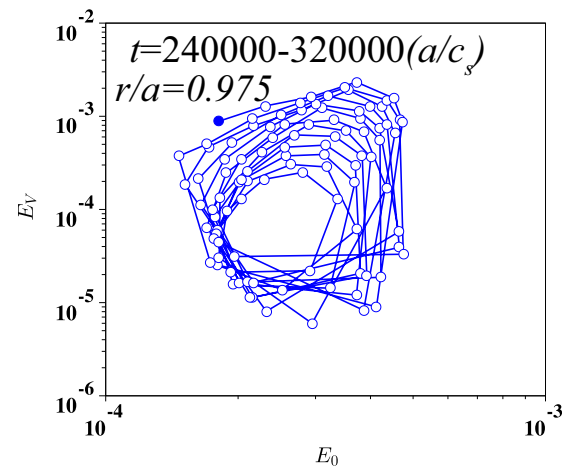


FIG. 3. Plots of ZF energy E_0 versus MF shearing energy E_V . Data points are taken from $t = 2.4 \times 10^5(a/c_s)$ to $t = 3.2 \times 10^5(a/c_s)$ with each $\Delta t = 8 \times 10^2(a/c_s)$. (The number of plots is 100.) The plots exhibit the limit-cycle oscillations. The propagating nonlinear waves are locally the limit-cycle oscillations with a phase delay between different radii. The filled circular plot denotes the final point at $t = 3.2 \times 10^5$. It indicates that the limit cycle rotates counterclockwise.

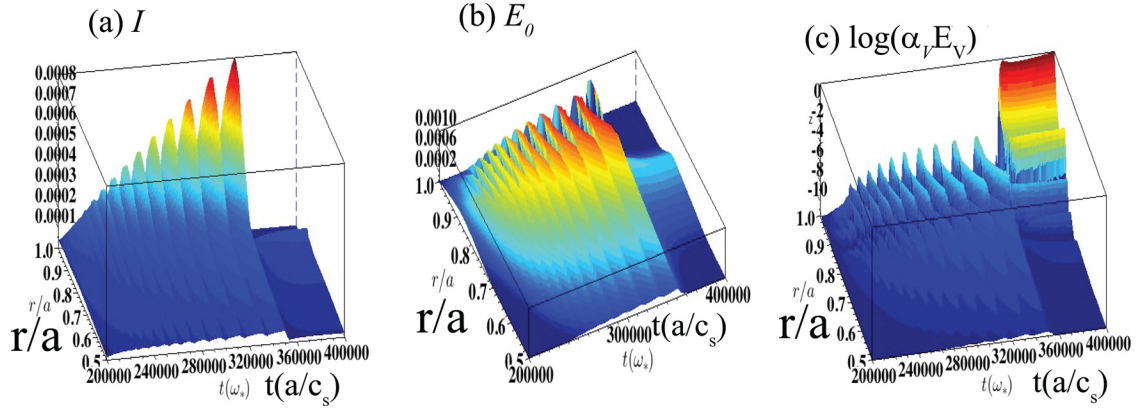


FIG. 4. Three-dimensional color maps of the time evolution of (a) turbulence intensity I , (b) ZF energy E_0 , and (c) MF shearing energy $\ln(E_V)$ as functions of time t (during the slow power ramp regime ($2 \times 10^5 < t < 4 \times 10^5$)) and radius ($0.5 < r/a < 1.0$). These pictures show nonlinear waves propagating inward from the edge layer as the transition develops. What locally appears as a limit cycle is actually a slice of propagating nonlinear wave in the edge layer.

as Fig. 2. We see that the LCO is a propagating nonlinear wave of turbulence, ZF, and MF shear fields in the edge layer around $r/a > 0.85$. The mean flow shear, representing the profiles, oscillates during I-phase. This is likely related to the oscillation of D_α signal observed in experiments. The local maximum of turbulence intensity peaks just prior to the transition.

Fig. 5 shows time evolution of turbulence intensity, ZF, and MF energies at various radial locations at the edge region ($r/a = 0.975, 0.950, 0.925$). Inward propagation of MF shear is identified. We notice that as the heat flux approaches criticality, the LCO phase delay between I and E_0 increases from $\sim \pi/2$ to $\sim \pi$, while the nonlinear LCO period *increases*, i.e., the cycle slows. Interestingly, this tendency is seen in the local model¹³ and also in DIII-D.¹⁷ In the DIII-D experiments in L-mode, no correlation of MF shear and turbulence is seen. During the LCO a $\pi/2$ phase shift is found, and the phase shift approaches $\sim \pi$ at final H-mode

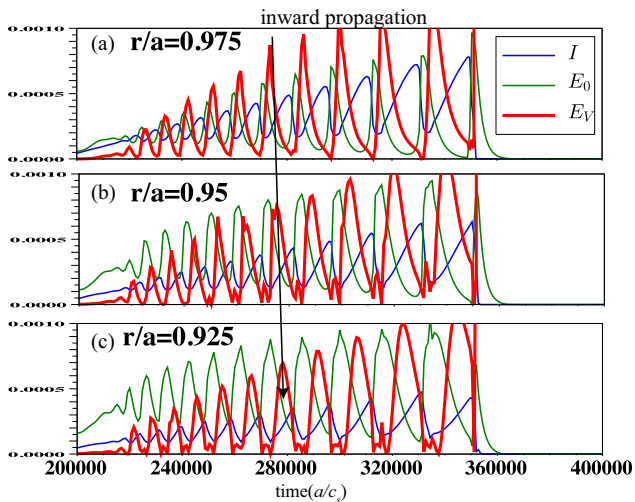


FIG. 5. Time evolution of turbulence intensity I (blue solid line), ZF energy E_0 (green solid lines), and mean square MF shear E_V (red bold lines) at various radial location of (a) $r/a = 0.975$, (b) $r/a = 0.950$, and (c) $r/a = 0.925$. The arrow indicates inward propagation of the mean flow peaks. At constant phase, the innermost radius leads in time, suggesting inward propagation.

transition, as equilibrium flow shear quenches the Reynolds stress.

Fig. 6 shows the evolution of MF and ZF shearings through $L \rightarrow I \rightarrow H$ transition, so as to compare with recent experimental results. Fig. 6(a) shows the temporal evolution of the diamagnetic shearing, i.e., $\omega_{E \times B, \text{dia}} = L_n^{-1} L_p^{-1} (c_s \rho_i)$. The diamagnetic shear oscillates with growing amplitude in I-phase, then increases abruptly at $L \rightarrow H$ transition. This is consistent with experimental results.¹⁷ This indicates that pressure and density gradients oscillate during I-phase, since the diamagnetic shear does. The oscillation of the density gradient must be related to D_α signal oscillations in experiments.

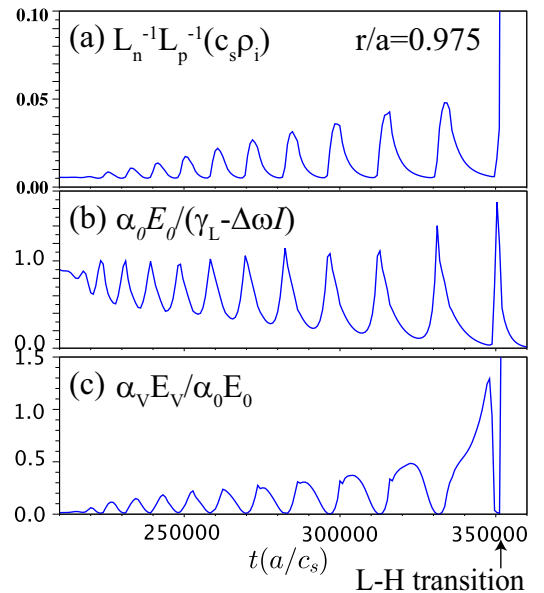


FIG. 6. Time evolution of (a) diamagnetic shearing (the first term of Eq. (13)), (b) η , i.e., the ratio of turbulence energy transfer to the ZF, normalized to the net energy input into the turbulence, and (c) the ratio of MF shear to ZF shear, from the onset of I-phase at $t = 2.1 \times 10^5 (a/c_s)$ to the L-H transition indicated at $t = 3.5 \times 10^5 (a/c_s)$ at the edge region $r/a = 0.975$. Throughout the I-phase, diamagnetic shearing oscillates with increasing amplitude. At the last cycle at $t = 3.5 \times 10^5 (a/c_s)$, ZF shearing is strongly enhanced, and sufficient to quench the turbulence. Then the mean shear is sufficient to lock in the transition.

A. Studies of a ZF role in the L → H transition: Triggering

Next, we investigate how ZF shearing mediates the L → H transition. In order to clarify the parameters which we will use, it is useful to write a schematic set of coupled predator-prey equations^{13,41} for turbulence and ZF, which are a simplified version of Eqs. (1) and (2), neglecting mean flow and nonlocal effects. These are

$$\frac{\partial I}{\partial t} = \gamma_{\text{eff}} I - \langle \tilde{v}_r \tilde{v}_\theta \rangle \frac{\partial v_{\text{ZF}}}{\partial r}, \quad (18)$$

$$\frac{\partial E_0}{\partial t} = \langle \tilde{v}_r \tilde{v}_\theta \rangle \frac{\partial v_{\text{ZF}}}{\partial r} - \gamma_{\text{damp}} E_0. \quad (19)$$

Here $\gamma_{\text{eff}} = \gamma_L I - \Delta\omega I^2$ is a total, effective growth rate, including the gradient drive and nonlinear damping.

$$\mathcal{P}_\perp = \langle \tilde{v}_r \tilde{v}_\theta \rangle \frac{\partial \langle v_{\text{ZF}} \rangle}{\partial r} \sim \alpha_0 I E_0 \quad (20)$$

is the Reynolds work of the fluctuations on the flow. $\langle \tilde{v}_r \tilde{v}_\theta \rangle \sim \pm \partial v_{\text{ZF}} / \partial r$ indicates negative (i.e., ZF growth) or positive (i.e., ZF damping) viscosity, respectively.

The obvious criterion for triggering the L → H transition is $\partial I / \partial t < 0$, with a positive phase between $\langle \tilde{v}_r \tilde{v}_\theta \rangle$ and $\partial v_{\text{ZF}} / \partial r$ —i.e., negative viscosity which results in a net decay of the fluctuation energy. In this case, the zonal flow extracts energy from the turbulence faster than the turbulence grows. This requires

$$\eta \equiv \frac{\langle \tilde{v}_r \tilde{v}_\theta \rangle \frac{\partial v_{\text{ZF}}}{\partial r}}{\gamma_{\text{eff}} I} = \frac{\alpha_0 E_0}{\gamma_L - \Delta\omega I} > 1, \quad (21)$$

which emerges as a natural figure of merit for the collapse of the turbulence and the onset of transition. Note that $\eta > 1$ does not always guarantee triggering of the L → H transition. This is *not a sufficient condition* but is at least the necessary condition to trigger the L → H transition by the zonal flow and mean flow interaction. In Ref. 41, results from “measurements” of η defined as $\mathcal{P}_\perp / \nu_{\text{net}} \langle \tilde{v}^2 \rangle$, instead of $\gamma_{\text{eff}} I$, were reported, where ν_{net} is the effective rate of energy input into the turbulence during periods of weak ZF. Results indicated that when η exceeds order unity, the L → H transition is triggered in EAST experiments.⁴¹ This shows that the ZF is *fundamental* to L → H transition, at least in those cases. Thus, we here compare the experimental results with numerical results based on the model presented here.

Fig. 6(b) shows the time evolution of η , indicating that peaks of the ZF shearing increase significantly close to L → H transition, consistent with the analyses from the experiment. This suggests that ZF shearing really becomes dominant just prior to the L → H transition. Fig. 6(c) shows a time evolution of MF shearing normalized by the ZF shearing. The MF shear starts to grow *after* the onset of the I-phase. In accord with the LCO, the normalized MF shear oscillates with growing amplitude. The size of this oscillation is largest just prior to the L → H transition. After the final peak of the MF shearing just prior to the transition, the MF shear rapidly drops and then increases, crossing zero. Finally, in the

H-mode pedestal, the MF shearing becomes much stronger than the ZF shearing.

Through Figs. 6(a)–6(c), we present the sequence for the development of the transition. Initially, the MF shear rapidly decreases and then increases in Fig. 6(c), followed by peaking of η in Fig. 6(b), and then $\omega_{E \times B, \text{dia}}$ increases rapidly. The MF first peaks and then collapses to small value as L_p^{-1} drops. The ZF then peaks and extracts the energy from the turbulence. L_p^{-1} and L_n^{-1} then increase rapidly as do the MF and the $\omega_{E \times B, \text{dia}}$. This sequence of the events explicitly demonstrates the causality of the transition! Noting that *the peak of η precedes the rapid increase of $\omega_{E \times B, \text{dia}}$, and the increase of $\omega_{E \times B, \text{dia}}$ must precede the decrease of D_α in experiments*, we conclude that the peak of η , which is related to the ZF shearing, is the trigger of the L → H transition.

The ZF plays a role of an energy *reservoir*, mediating the transition by absorbing free energy without increasing turbulent transport. The zonal flows act as *short time storage place* for most or all of the fluctuation energy in a region of the spectrum which causes no transport (i.e., $n=0$). This allows the mean flow shear to increase (due to profile steepening), so the transition can develop. *The actual L → H transition occurs when the instantaneous LCO ZF shear is sufficient to quench the turbulence by momentarily extracting essentially all of the energy out of the turbulence, thereby allowing rapid growth of the mean shear, which then locks in the transition.*

B. Studies of the general L → H transition with a fast ramp of heat flux

The rate of heat flux increase, related to the rate of increase of power, can be another factor which determines “the type of L → H transition.” We know that there are actual cases for which the L → H transition occurs *without* an I-phase. The answer to the question comes from considering the rate of the heat flux increase. Indeed, the I-phase was only identified by carefully creating experiments operating near the power threshold. To this end, we examine the case with a *faster* power ramp, shown in Figs. 7(a)–7(c). In this case, the LCO is compressed into a single burst of ZF, which triggers L → H transition at $t = 2.7 \times 10^4 (a/c_s)$. For the single burst scenario to apply the heat flux increase, time scale must be shorter than the time scale of a single limit-cycle. While turbulence is quenched immediately after the L → H transition is triggered, the ZF is damped more slowly, in accord with the modest ZF damping time ($\sim \gamma_{\text{ZF}}^{-1}$). These features seen in Figs. 7(a)–7(c) resemble those of TJ-II, shown in Fig. 7 of Ref. 42. A small increase of the MF shearing in accord with the burst of ZF in $0.65 < r/a < 1.0$ and $2.3 \times 10^4 (a/c_s) < t < 2.7 \times 10^4 (a/c_s)$ is seen in Fig. 7(c). This indicates that the ZF induces MF growth through turbulence suppression.

We discuss the trigger of the L → H transition without the I-phase, using the parameter η in Eq. (21). In Figs. 7(d)–7(f), temporal evolutions of turbulence intensity I , ZF energy E_0 , MF energy E_V , the product quantities $\mathcal{P}_\perp = \alpha_0 I E_0$, and $\eta = \alpha_0 E_0 / (\gamma_L - \Delta\omega I)$ are shown at a specific radial location $r/a = 0.9625$. To make clear the sequence of events

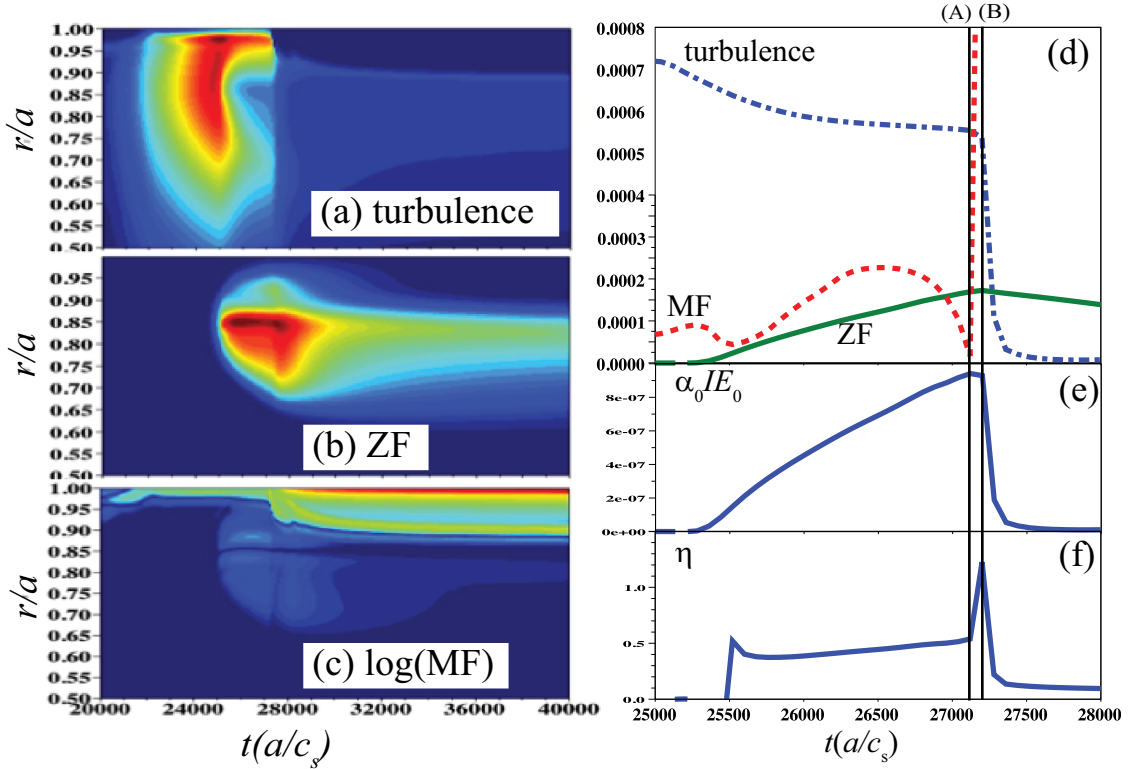


FIG. 7. Spatio-temporal evolution of turbulence (a) I , (b) E_0 , and (c) $\ln(E_V)$ as a function of time t during a fast power ramp $2 \times 10^4 (a/c_s) < t < 4 \times 10^4 (a/c_s)$, and radius ($0.5 < r/a < 1.0$). No LCO is seen. The I-phase LCO is compressed into a single burst of ZF at $t = 2.72 \times 10^4 (a/c_s)$. (d) Time evolution of turbulence intensity I (blue chain line), ZF energy E_0 (green solid line), and MF shearing energy E_V (red dotted line). This figure shows that at the L \rightarrow H transition $t = 2.72 \times 10^4 (a/c_s)$, the turbulence quenches at a faster rate, the ZF increases before the transition and damps after the transition, and MF shear rapidly increases at and just after the transition. (e) The evolution of the product quantity $\mathcal{P}_\perp = \alpha I E_0$. The product quantity exhibits a peak just before the transition and quenches after the transition. (f) An evolution of η , showing a single burst at $t = 2.72 \times 10^4 (a/c_s)$. This single burst triggers the quench of turbulence and the product quantity $\alpha_0 I E_0$. Thus, the L \rightarrow H transition occurs. For convenience, we here draw vertical lines (A) at $t = 2.71 \times 10^4 (a/c_s)$ and (B) at $t = 2.72 \times 10^4 (a/c_s)$.

occurring during the L \rightarrow H transition, we denote vertical lines (A) and (B) on Figs. 7(d)–7(f). At the time (A), i.e., just prior to the L \rightarrow H transition, MF shear crosses zero and then exhibits a rapid increase. Simultaneously, the product \mathcal{P}_\perp shows a peak, and η increases rapidly. At the time (B), i.e., just at the time of L \rightarrow H transition, turbulence drops rapidly, so \mathcal{P}_\perp also drops proportional to the behavior of the turbulence intensity. A single peak of η is also identified at the time (B). The peak is due to an increase of ZF shearing and also transient drop of γ_L . The transient drop of γ_L originates from the rapid decrease of L_T^{-1} . The decrease of L_T^{-1} appears coincident with the decrease of MF shear at the time (A). Thus, the sequence in which the L \rightarrow H transition is triggered here is consistent with the case with slow ramp, seen in Fig. 6.

C. Basic properties of density, pressure, turbulence intensity, zonal flow, and mean flow shear in L-mode, I-phase, and H-mode

In this subsection, we show further analyses obtained from the case with a slow power ramp. The condition is the same as that in Fig. 2. Fig. 8 shows spatial evolutions of density, pressure, and temperature profiles at typical times of the L-mode, I-phase, and H-mode. Pedestal formation in the H-mode is clearly recovered in the edge region, $0.9 < r/a < 1.0$. Note that these profiles including pedes-

tals are not empirically specified, but rather evolve given by the time evolution of the self-consistent theoretical model.

In L-mode or I-phase, both heat and particle diffusivities in the edge region are governed by turbulent transport, since the relation $D_{n.t.}, \chi_{n.t.} \ll D_0, \chi_0$ is satisfied. On the other hand, in the H-mode pedestal, the diffusivities are governed by the non-turbulent transport instead, due to the quench of turbulence. Once the L \rightarrow H transition occurs, the diffusivities in the pedestal region drop immediately. As a consequence steep profile gradients are formed, and the MF shear is rapidly excited. On the pedestal shoulder, residual turbulence and ZF persist. They round off the profiles at the top of the pedestal after the L \rightarrow H transition, thus leading to formation of a convex pedestal corner.

We focus on the profile in the edge region as seen in Fig. 9. The pressure profile in I-phase at $t = 2.8 \times 10^5 (a/c_s)$ is not peaked in the edge region, compared to that in L-mode. There is some enhanced turbulence because of the decorrelation of ZF shearing by the MF shear, leading to stronger turbulent transport. Judging from Fig. 5(a), at $t = 2.8 \times 10^5 (a/c_s)$ in the edge region $r/a > 0.95$, turbulence is most enhanced and thus the ZF and MF shear exhibit minima. Therefore, the profile behaves like an L-mode, with minimum flow shearing. For the contrary phase, at $t = 2.72 \times 10^5 (a/c_s)$, turbulence is minimal, and the ZF and MF shear are enhanced. Thus, a steeper gradient than that in

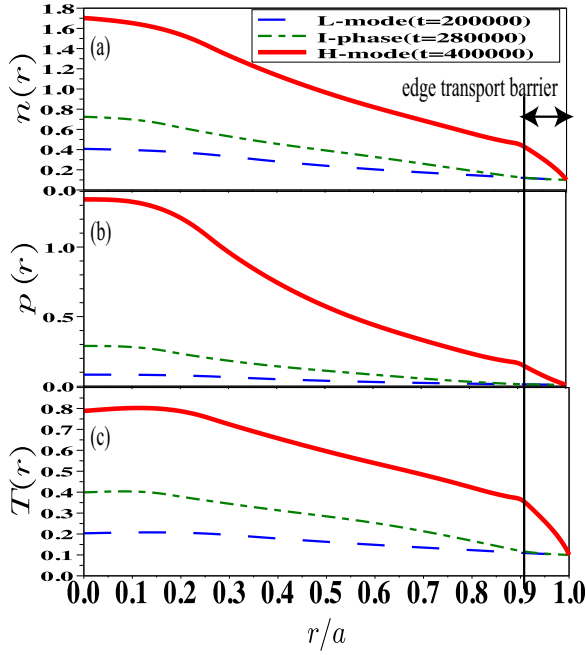


FIG. 8. Profiles of (a) density $n(r)$, (b) pressure $p(r)$, and (c) temperature $T(r)$ at times of L-mode (blue dashed line) $t = 2.0 \times 10^5 (a/c_s)$, I-phase (green chain line) $t = 2.8 \times 10^5 (a/c_s)$, and H-mode (red solid bold line) ($t = 4.0 \times 10^5$), respectively, as a function of radius ($0.0 < r/a < 1.0$). This is for the case of a slow power ramp. At $r/a = 0.9$, a significant edge transport barrier in H-mode appears, as indicated by the vertical line.

L-mode is observed. This is how the profile oscillates in I-phase.

Fig. 10 shows the spatial evolution of turbulence intensity, ZF, and MF energies. Turbulence is quenched in the H-mode pedestal. Consequently, in Fig. 10(b), in H-mode, the ZF is eliminated from the pedestal, except at the pedestal shoulder. ZF is enhanced around $r/a \sim 0.85$ but decreases in the edge region for $r/a = 0.9 - 1.0$, in correspondence to the increase of turbulence, due to decorrelation of ZF shearing by MF shearing. In Fig. 10(c), MF shear exhibits significant

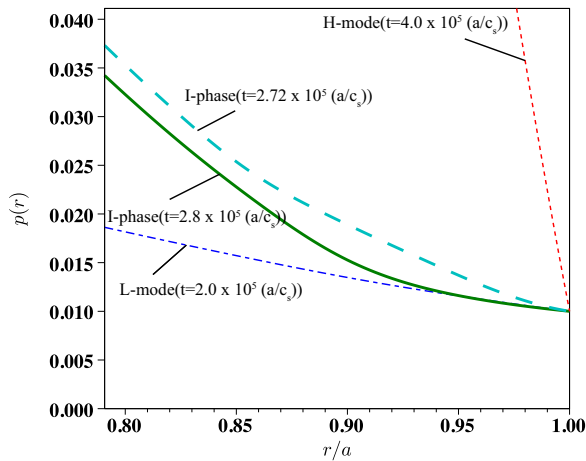


FIG. 9. Comparison of profiles of $p(r)$ at times of L-mode $t = 2.0 \times 10^5 (a/c_s)$, H-mode $t = 4.0 \times 10^5 (a/c_s)$, and I-phase with different phase $t = 2.72, 2.8 \times 10^5 (a/c_s)$, on $0.8 < r/a < 1.0$. At $t = 2.8 \times 10^5 (a/c_s)$, turbulence is peaked at the edge. Thus, the profile gradient flattens in the edge region $0.95 < r/a < 1.0$. At $t = 2.72 \times 10^5 (a/c_s)$, in turn, in the edge region, turbulence shrinks and mean flow is most enhanced. Thus, a steeper profile gradient is observed.

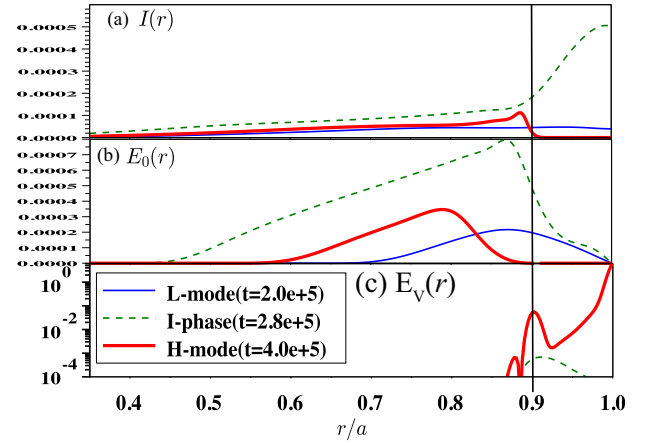


FIG. 10. Profiles are shown for (a) turbulence intensity $I(r)$, (b) ZF energy $E_0(r)$, and (c) MF shearing energy E_V at times of L-mode $t = 2.0 \times 10^5$, I-phase $t = 2.8 \times 10^5 (a/c_s)$, and H-mode ($t = 4.0 \times 10^5$), respectively, as a function of radius ($0.35 < r/a < 1.0$) for the case of slow power ramp up. At $r/a = 0.9$, the vertical line indicates the region where the edge transport barrier is established. H-mode is characterized by an enhanced MF shear and quench of turbulence intensity, and ZF shearing in the edge region, $r/a > 0.9$. In L-mode, the MF shearing contribution is negligible, while in I-phase, a propagating MF structure is observed.

structure in the pedestal. The MF shear in the H-mode pedestal is much stronger than the ZF shear. In the I-phase, MF shearing oscillations are seen as part of the LCO propagation. In the L-mode, MF shearing contribution is negligible.

Fig. 11 shows profiles of diamagnetic shearing (the first term of Eq. (13)), pressure profile curvature (the second term of Eq. (13)), poloidal flow shearing (the fourth term of Eq. (13)), and neoclassical poloidal flow shearing ($\langle v_\theta^{(neo)} \rangle'$ in Eq. (12)) for the I-phase and the H-mode. These parameters are the ingredients of the mean flow shearing. As seen in Fig. 11(a), in I-phase, the main contributor to the mean flow shear in the edge region is the poloidal flow, which is mostly neoclassical, except for a very thin layer within the thin pedestal. The pressure curvature is comparable to the diamagnetic shearing, indicating that analyses without the pressure curvature are not valid. The radial structure of the pressure profile curvature appears to be out of phase with the poloidal flow. The fine structure of the MF shearing driven by the pressure curvature and neoclassical poloidal flow may be related to the nonlinear wave propagation discussed previously, since profiles of the diamagnetic shearing without the second derivative of profile stay constant through I-phase.

In H-mode, shown in Fig. 11(b), the diamagnetic shear dominates the mean flow shearing in the pedestal, while the profile curvature contribution in the pedestal is not significant. Because of the quench of the turbulence in the pedestal, the poloidal flow is mostly governed by the neoclassical contribution. At $r/a = 0.90$, pedestal corner forms, so the curvature contribution is necessarily important there. This result is also consistent with the argument in Ref. 35. While the turbulence driven poloidal flow is localized at the thin edge layer, the poloidal flow profile is mostly neoclassical, as seen in Fig. 11(b). This is, however, dependent on the neoclassical poloidal viscosity, proportional to ν_{ii} . Therefore, the situation may be different for lower ν_{ii} .

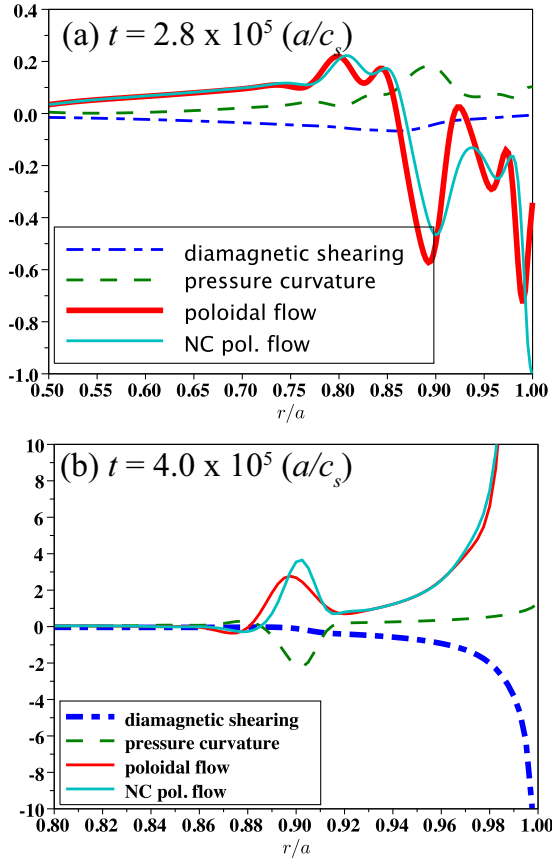


FIG. 11. Profiles of diamagnetic shearing $-L_p^{-1}L_n^{-1}(\rho_i c_s)$ (blue chain line), pressure profile curvature $L_p^{-1}L_p^{-1}(\rho_i c_s)$ (green dash line), poloidal flow shearing $(v_\theta)'$ (red solid line), and neoclassical poloidal flow shearing $(v_\theta^{(neo)})'$ (light green solid line) for times of I-phase ($t = 2.4 \times 10^5 (a/c_s)$) and (b) H-mode ($t = 2.8 \times 10^5 (a/c_s)$), respectively, for the case of a slow power ramp. Here, we show all quantities used in the radial force balance equation Eq. (14) and poloidal flow evolution equation, Eq. (12). In the case of I-phase, neoclassical poloidal flow and pressure curvature are the dominant players in MF shearing, while in the case of H-mode, neoclassical poloidal flow and diamagnetic shearing are the dominant players in the pedestal ($0.90 < r/a < 1.0$), but pressure curvature can be large at the pedestal shoulder, around $0.88 < r/a < 0.92$.

IV. NEUTRAL DENSITY AND FUELING EFFECTS ON TRANSITION AND THE PEDESTAL

In this section, we first show results of numerical studies of tests on the $L \rightarrow H$ power threshold for various ZF damping and poloidal viscosity. These tests represent variable neutral density effects. As is widely known, high edge neutral density is unfavorable to the transition.²² While this may be due to higher radiation reducing confinement, increased ZF damping is also a possibility. We here re-visit the issue of neutral related problems in relation to the ZF damping rate. We investigate studies with a higher ZF damping rate, corresponding to cases with higher edge neutral CX friction. Next, we discuss fueling effects on the density profile. By changing the fueling depth with and without the particle pinch effect, we discuss how the pedestal width can vary.

In Fig. 12, we show cases with various ZF damping rates $\gamma_{\text{damp},0} = 1, 2, 3$ and neoclassical viscosities $\mu_0^{(neo)} = 0.5, 1, 1.2$. Here, the ZF damping rates and the neoclassical viscosities are normalized by ν_{ii}/R and $\nu_{ii}q^2R^2$, respectively. We here fix the

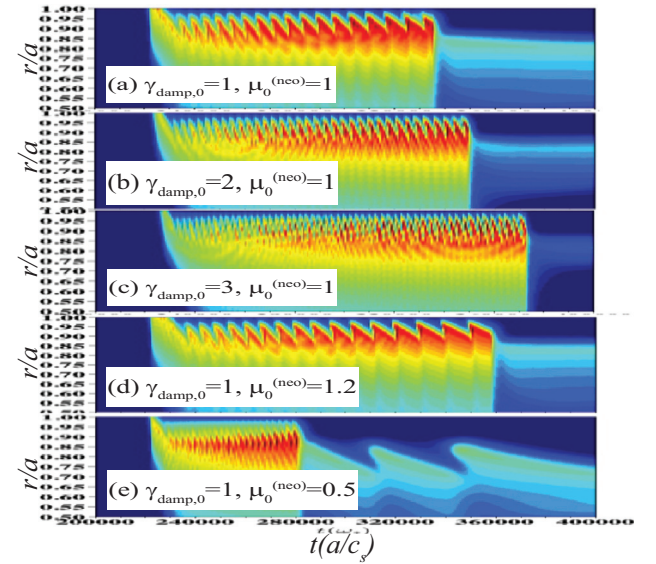


FIG. 12. Spatio-temporal evolution of ZF energy E_0 in cases with a fixed slow heat flux power ramp and various ZF dampings $\gamma_{\text{damp},0} = 1, 2, 3$ and neoclassical viscosities $\mu_0^{(neo)} = 0.5, 1, 1.2$. (a)–(c) show cases with fixed $\mu_0^{(neo)}$, but increasing $\gamma_{\text{damp},0}$. Increase in $\gamma_{\text{damp},0}$ is followed by delays of the transition. (a) and (d) and (e) show cases with fixed $\gamma_{\text{damp},0}$, but varying $\mu_0^{(neo)}$. As $\mu_0^{(neo)}$ increases, the transition occurs later.

ramp speed slow, which is the same case as Fig. 2. As seen in Figs. 12(a)–12(c), the transition delays as the ZF damping rate increases, with fixed neoclassical viscosity. Thus, the power threshold increases as the ZF damping increases. The period of LCO decreases as the ZF damping increases. This indicates that the period of the LCO depends on the ZF damping rate, a tendency which is consistent with the original model of Ref. 13. A similar tendency to delay transition can be found in comparison with different $\mu_0^{(neo)}$ and the fixed ZF damping rate, as seen in Figs. 12(a), 12(d), and 12(e). Delays of the transition are also observed when the neoclassical viscosity $\mu_0^{(neo)}$ increases. The period of LCO decreases as the neoclassical viscosity $\mu_0^{(neo)}$ decreases. This is because more poloidal velocity shear, driven by turbulence, is excited in the lower $\mu_0^{(neo)}$ and thus more MF shear, instead of the ZF shearing, affects the turbulence intensity evolution. Thus increasing either the ZF damping or the neoclassical viscosity delays transition at constant heat flux power ramp, causing a power threshold upshift.

Fig. 13 shows plots of the power thresholds $Q_{a,\text{crit}}$ obtained from numerical tests with various ZF damping rate $\gamma_{\text{damp},0}$ and neoclassical poloidal viscosity $\mu_0^{(neo)}$, for a fast power ramp. It is clear that the power threshold increases as either ZF damping or neoclassical poloidal viscosity increases. Thus, we expect higher neutral CX to increase the power threshold. This is not surprising, since ZF shearing is fundamental to the transition. Increasing ZF damping reduces ZF shearing and its effect on the suppression of turbulence, leading to an upshift in the transition threshold. We note that recent XGC1 simulations with neutrals found results which suggested damping of zonal flows by neutral drag.⁴³

We examine the cases without ZF shearing, i.e., $\alpha_0 = 0$, with various neoclassical viscosities. Without the ZF shearing, the $L \rightarrow H$ transition occurs when $\mu_0^{(neo)} \leq 0.5$.

$Q_{a,crit} = 0.0013$ is obtained when $\mu_0^{(neo)} = 0.5$ and $Q_{a,crit} = 6.7 \times 10^{-3}$ is obtained when $\mu_0^{(neo)} = 0.1$. These power thresholds are asymptotic to those in the cases with higher ZF damping, $\gamma_{damp} = 10$ with the same $\mu_0^{(neo)}$, plotted in Fig. 13. Cases with higher ZF damping asymptotically approach the case with no ZF shearing. We estimate the power threshold without ZF shearing. In cases with $\mu_0^{(neo)} = 0.1, 0.5$, the power threshold without ZF shearing is found to approach the cases with higher ZF damping, i.e., $\gamma_{damp,0} = 10$. For cases with $\mu_0^{(neo)} > 1.0$ and $\gamma_{damp} > 5$, the transition does not occur during the power ramp to $Q_a < 0.05$. At least in these cases, the power threshold without ZF shearing increases drastically. This observation supports the hypothesis that the zonal flow is fundamental to the $L \rightarrow H$ transition.

An important question here is whether the $L \rightarrow H$ transition can occur without ZF shearing. According to the local predator-prey model analyses,¹⁹ without ZF shearing, the $L \rightarrow H$ transition can still occur with a sufficiently high level of the heat flux. The QH state exists in any power level of the heat flux and is stabilized above a power which is sufficient to excite the mean flow shear. The L state cannot exist above a certain heat flux, due to strongly excited mean flow. The fundamental role of ZF shearing in the $L \rightarrow H$ transition is to reduce the power threshold by reducing the turbulence level. However, with higher ZF damping, there is no significant difference in the turbulence level, with or without ZFs. Therefore, the power threshold with higher ZF damping can be asymptotic to that without ZF shearing.

We study fueling effects on the transition and pedestal structure, with special focus on the particle pinch. In Fig. 14, we plot the calculated power thresholds $Q_{a,crit}$ with ($V_{n0} = 1.0$) and without ($V_{n0} = 0$) particle pinch, and with various fueling deposition widths $L_{dep} = 0.05 - 0.20$. The power thresholds with particle pinch are higher, as compared with those without particle pinch. Either with or without the

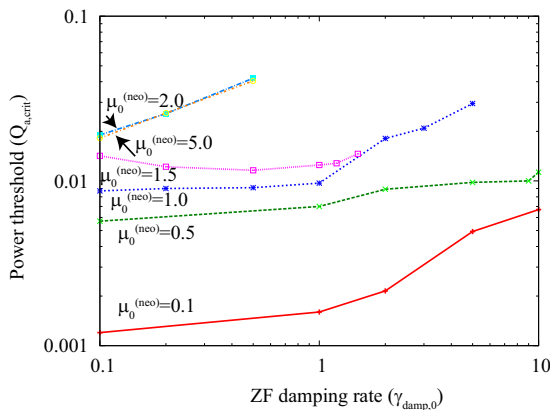


FIG. 13. Investigation of power threshold $Q_{a,crit}$ for various ZF damping rates $\gamma_{damp}^{(neo)}$ as well as for neoclassical poloidal flow viscosities $\mu_0^{(neo)}$. In cases with $\mu_0^{(neo)} \geq 2.0$, no transition occurs for $Q_a < 0.05$. In case of $\mu_0^{(neo)} = 1.5$ and $\gamma_{damp}^{(neo)} > 2.0$, the transition does not occur for $Q_a < 0.05$. In cases with $\mu_0^{(neo)} = 1.0$ and $\gamma_{damp} > 1.0$, the transition does not occur for $Q_a < 0.05$. In case of $\mu_0^{(neo)} = 0.5$, and $\gamma_{damp} = \infty$, i.e., without ZF shearing ($\alpha_0 = 0$), the transition occurs at $Q_a = 0.013$. In case of $\mu_0^{(neo)} = 0.1$, without ZF shearing, the transition occurs at $Q_a = 6.7 \times 10^{-3}$, which power threshold is equivalent to the case of $\mu_0^{(neo)} = 0.1$ and $\gamma_{damp} = 1.0$.

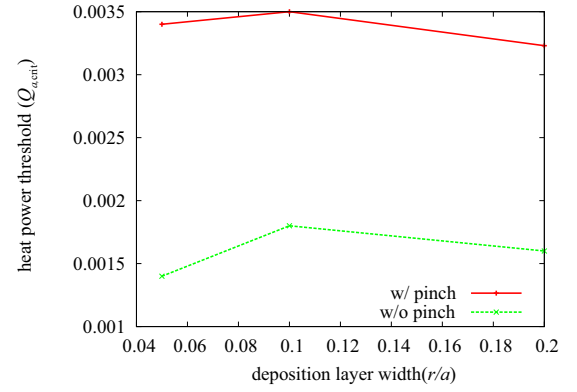


FIG. 14. Plots of power threshold $Q_{a,crit}$ for various deposition layer width L_{dep} with and without particle pinch effects. The power threshold with particle pinch are higher than that without particle pinch. Either with or without the particle pinch, little sensitivity is found in the power threshold for various deposition layer widths.

particle pinch, there is little difference in power threshold for various fuel depositions. To discuss more about the effects of particle pinch, we show profiles of turbulence intensity with and without the particle pinch in Fig. 15. Comparing cases with and without the pinch, there is no qualitative difference in the turbulence profile. However, the turbulence intensities are different because of different γ_L , as the particle pinch effectively reduces the temperature gradient. This is because the particle pinch tends to steepen the density gradient, and since the pressure gradient is approximately constant, $|L_T|^{-1} = |L_p|^{-1} - |L_n|^{-1}$, the temperature gradient necessarily decreases. As turbulence is thus more weakly excited, ZF

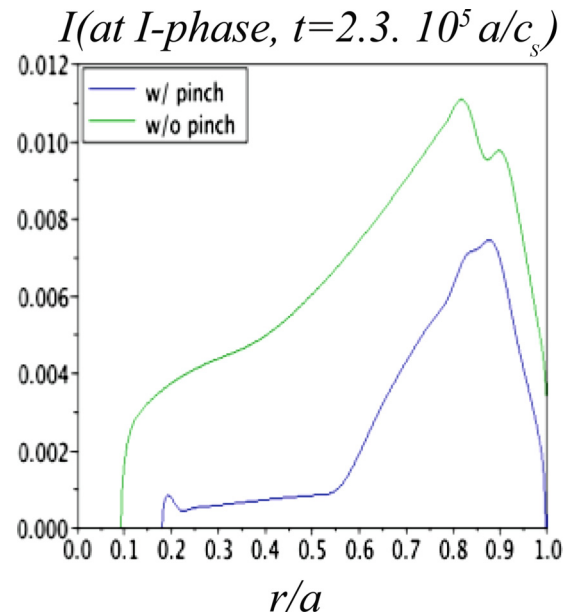


FIG. 15. Profiles of the turbulence intensity in cases with the pinch (blue) and without pinch (green) effects during I-phase, $t = 2.3 \times 10^5 (a/c_s)$. This shows that more turbulence exists in the case without the pinch effects than for the case with the pinch effects. The stronger turbulence in cases without the pinch effects excites more ZF shearing. The ZF shearing triggers $L \rightarrow H$ transition at lower power thresholds.

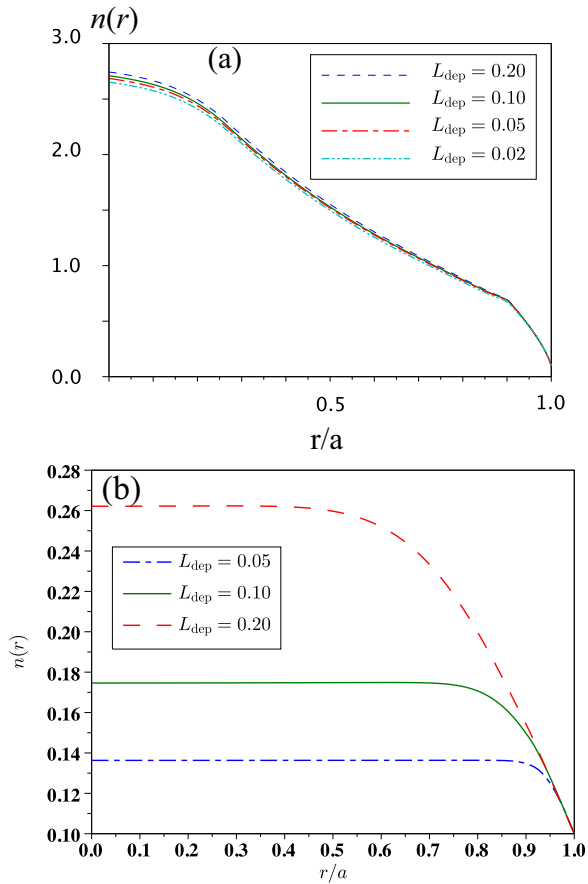


FIG. 16. Density profiles in H-mode with various fueling deposition layer width L_{dep} and (a) with and (b) without particle pinch. In (a), little difference results from changing the fueling deposition layer width, while in (b), the pedestal width increases as the fueling width increases. Flat profiles and much lower core density quantities are obtained in case without the pinch.

excitation drops too, so a higher power threshold can be expected. Note that with pinch effects, a much larger core density is also achieved, as compared to the case without a pinch. The higher density may induce higher radiation or ZF damping due to the CX friction. This may further increase the power threshold. Further studies are left to the future, but at least we expect a significant effect of the density pinch on the power threshold.

Here, we discuss effects related to the extent of the fueling deposition width. As is discussed above, in both cases with and without particle pinch, the fueling depth has little effect on the power threshold, as seen in Fig. 14. However, pedestal formation in the early stage of H-mode exhibits different features. In Fig. 16, we show pedestal structure of density profiles in H-mode with and without particle pinch and with various fueling deposition widths L_{dep} . With particle pinch and increasing the fueling depth, there is little difference in pedestal width, as seen in Fig. 16(a). However, without the particle pinch, an increase in the fueling depth causes an increase of pedestal width, as seen in Fig. 16(b). It is interesting to note that the density gradients in the pedestal are similar to those for fixed fueling source strength, while the core density increases as the pedestal width increases. Inward from the pedestal, density profiles are flat without the particle pinch. One reason why there is little dependence of

the fueling width on the particle pinch is that the peaking effect of the particle pinch may be overestimated and thus may overwhelm the fueling.

V. CONCLUSION

We have investigated the space-time evolution of the $L \rightarrow H$ transition, using a time-dependent, one dimensional mesoscale model which self-consistently describes the evolution of turbulence intensity, ZF, density and pressure profiles, and mean poloidal mass flow. The model captures the essential physics of ZF and MF interaction, turbulence suppression by ZF and MF shearing, and poloidal flow evolution, including that driven by turbulence. We here have elucidated how ZF shearing mediates the transition. These findings are in good agreement with findings from several DBS^{17,20,42} and probe experiments^{18,41} and point to the crucial role of ZFs in the transition dynamics. The specific results of this study are as follows:

- I. Studies with a slow power ramp have manifested an $L \rightarrow H$ transition via I-phase, characterized by a series of nonlinear waves, which, locally, are LCOs. The I-phase nucleates near, but not at the LCFS. In the model, the MF shear peak nucleates at the fixed edge boundary. This result, a consequence of boundary conditions, should be compared with results from DIII-D, where the total $E \times B$ flow velocity negative well nucleates in the edge region and rises to be positive outside of the LCFS.
- II. The I-phase is a multi-predator-prey oscillation of turbulence intensity, zonal flow, and mean flow shear. The LCO is part of an inward propagating nonlinear wave and appears as a slowly oscillating region of growing width. Mean flow shear growth begins *after* the onset of I-phase.
- III. As is seen in DIII-D, the LCO period increases approaching the transition. The I-phase terminates abruptly at transition, with rapid growth of MF shear. At the transition, pedestals in density and temperature begin to expand inward. Local turbulence intensity peaks just prior to transition. Mean flow shear locks in the transition in H-mode.
- IV. The phase delay between turbulence and zonal flow increases from $\pi/2$ to π during the I-phase, consistent with the 0D Kim-Diamond model¹³ and also DIII-D results. The diamagnetic shear oscillates with growing amplitude in I-phase, then increases abruptly at the $L \rightarrow H$ transition, as seen in DIII-D. The growth of the diamagnetic flow shear amplitude occurs only in I-phase, not in L-mode. The peak of the ZF shear increases just prior to transition. This is consistent with the analyses of EAST experiments, suggesting that ZF shearing is dominant just prior to the $L \rightarrow H$ transition.
- V. At the $L \rightarrow H$ transition, the MF first grows and then collapses to a small value as L_p^{-1} drops. The ZF then peaks and extracts the energy from the turbulence. Then, L_p^{-1} and L_n^{-1} increase rapidly, as does the MF. This is consistent with the analyses of EAST

experiments, suggesting that ZF shearing is dominant just prior to the $L \rightarrow H$ transition.

- VI. The actual transition event is abrupt, even if the power ramp and LCO evolve slowly. After the transition, edge pedestals in n , p , and also T form quickly. This picture is consistent with the experiments, in which the pedestal expands *after* the $L \rightarrow H$ transition.
- VII. Numerical studies reveal that two kinds of the transition are possible. With slow power ramp, $L \rightarrow H$ transition occurs via I-phase, which clearly manifests a quasi-periodic oscillation. On the other hand, during a fast power ramp, the I-phase is compressed into a single burst of ZF, leading to a transition without I-phase. Here, how *fast* the ramp must be so as to prevent I-phase depends on the ramp-up rate as compared to the period of the limit-cycle.

Studies of power threshold with various ZF damping and neoclassical poloidal viscosity indicate that *larger neutral CX increases the power threshold*. More generally, increasing ZF damping increases the power threshold, suggesting that ZF is fundamental to the transition. ZF can act as “reservoir” in which to store large fluctuation energy *without increasing transport*, thus allowing the mean flow shear to grow. Mean flow shear, however, ultimately is required to “lock in” the state of quenched turbulence. Therefore, the ZF damping must enter the power threshold condition but does not exclusively determine it. More systematic and quantitative studies of the power threshold require modification of mean flow evolution by SOL-edge interaction incorporating up-down asymmetry of X-point location in the single divertor configuration.⁴⁴ It is interesting to compare our present results to those of another model, which incorporates SOL and core interaction to formulate criteria that the $L \rightarrow H$ transition occurs.⁴⁵ The Fundamenski model does not address the temporal evolution of the $L \rightarrow H$ transition and also posits rather simplified core plasma dynamics. Nevertheless, it recovers certain experimental parameter scalings, including a bifurcation of the power threshold in density. Applying such SOL and core interaction conditions to the present model, we will explore estimation of the power threshold in a future study.

These results also suggest implications for future steady state experiments. We find that neutral CX can damp zonal flows in experiments,⁴⁶ indicating that high edge neutral density is unfavorable to transition. This can be related to the long established experimental lore concerning the power threshold, “dirty machines,” re-cycling, etc. The results have implication for the recovery of H-mode in steady state operation, if it is lost. In such the case of the recovery of H-mode, wall saturation and consequent increased re-cycling can ultimately lead to strong CX damping of ZFs, making it difficult to recover the H-mode should a back-transition occur. This suggest that proper wall conditioning, or reduction of wall impurity saturation, is necessary throughout the long pulse H-mode operation, because the ZF shearing necessary to trigger the transition may be more difficult to excite.

The trend that higher ZF damping increases the power threshold may explain the experimental scaling trend in the

higher density region, because $\gamma_{\text{damp}} \propto \nu_{ii} \propto n$. As well, increasing q may make a power threshold higher, since the neoclassical viscosity increases with q . B_T may change the power threshold through the change of ρ_i . We also note that according to Ref. 47, the simple model with Gyro-Bohm turbulence will give the power threshold $P_{\text{thresh}} \sim B_T^\alpha$, $1 < \alpha < 3$. Thus, the model finds that B_0 scaling in the power threshold appears from the ρ_i dependence of the coefficients. However, this result is mode dependent and needs further study.

Investigation of the transition and the pedestal structure, including dependence on density pinch and fueling deposition depth, has aimed to promote the understanding of the particle fueling dynamics. What we have found are the following:

- I. The density pinch reduces turbulence intensity and ZF shearing excitation, because the density peaking effect (due to the pinch) enhances reduction of the temperature gradient by the larger density gradient. This causes an upshift of the power threshold. With the particle pinch effect, the density profile can be peaked, and the *total* particle flux can be negative in the presence of a sufficiently steepened temperature gradient, assuming the ITG turbulence model.
- II. The fueling deposition depth has virtually no impact on the $L \rightarrow H$ transition, with or without particle pinch. Without particle pinch, deeper deposition makes a deeper density pedestal, while with particle pinch, little effects on the pedestal width are observed. This may be because here the peaking effects overwhelm the fueling effects.

For further parameter surveys to such cases where the external particle flux source and the pinch-induced peaking coexist, we need to expand the turbulence model to electron turbulence, such as CTEM. These will give more detailed physical insights for the fueling study and address such phenomena as gas-puffing, pellet injection, and also supersonic molecular beam injection (SMBI).

We remark on the relation of this study to high β plasma physics. We here do not consider electromagnetic physics such as kinetic ballooning mode (KBM) or peeling ballooning mode possibly excited in high β plasmas. Therefore, in the present model, we do not see any traditional ELM oscillations. Though KBM could play a role in determining the pedestal structure, KBM should not directly impact the $L \rightarrow H$ transition itself, since KBM is excited in higher β plasmas close to the ideal limit. For actual $L \rightarrow H$ transition physics—as opposed to *pedestal* physics—lower β plasmas are more relevant. Furthermore, we have already reproduced most of the detailed transition dynamics without considering high β physics.

In future work, we will study back transitions, i.e., $H \rightarrow L$ events. We note here some results, in relation to the ramp speed issue. Model studies of *slow* power ramp downs indicate that the $H \rightarrow L$ transition occurs via an I-phase. Instead, *fast* ramp downs exhibit a rapid burst of ZF activity, but no clear LCO. These features are similar as the phenomena, seen in the $L \rightarrow H$ forward transition. Furthermore, we will discuss effects of noise on the $L \rightarrow H$ transition in another work.

L \rightarrow H transition is fundamentally non-deterministic, as the edge layer bombarded by ensemble of core avalanches, producing large variability in the local heat flux. As edge heat flux variability is induced by core avalanches, the edge heat flux frequency spectrum is better taken to be $1/f$, i.e., pink noise, than white. $1/f$ noise is more effective for producing transitions than white noise, because $1/f$ noise tends to be more coherent. We will discuss these issues in future papers.

ACKNOWLEDGMENTS

The authors acknowledge stimulating discussions with G. Conway, J. Q. Dong, T. S. Hahm, C. Hidalgo, K. Ida, H. Jhang, Y. Kosuga, J. Lang, M. Malkov, P. Manz, D. C. McDonald, G. McKee, F. Ryter, M. Xu, X. Q. Xu, Y. Xu, Z. Yan, and K. J. Zhao. This work was supported by the WCI Program of the National Research Foundation of Korea funded by the Ministry of Education, Science and Technology of Korea [WCI 2009-001] and the Department of Energy under Award Number DE-FG02-04ER54738 and CMTFO.

APPENDIX A: THE DERIVATION OF THE FEEDBACK LOOP OF TURBULENCE, ZONAL FLOW, AND MEAN FLOW SHEARING

The derivation of the model to describe feedback loop between turbulence and ZF is shown here, taking into account multiple shearings such as MF. We start from the well-known wavekinetic equation⁴⁸ for drift wave action $N_k \equiv \epsilon_k/\omega_* \propto (1 + k_\perp^2 \rho_s^2) |\tilde{\phi}_k|^2$ and the zonal flow time evolution, where ω_* is drift wave frequency, and Doppler-shifted drift wave frequency $\omega_k = \omega_* + q_r V_{ZF}$, with respect to small-scale wave number \underline{k} and the radial wave number of mesoscale shear flows q_r and the zonal flow velocity V_{ZF} ,

$$\frac{\partial N_k}{\partial t} + \frac{\partial \omega_k}{\partial \mathbf{k}} \cdot \frac{\partial N_k}{\partial \mathbf{x}} - \frac{\partial \omega_k}{\partial \mathbf{x}} \cdot \frac{\partial N_k}{\partial \mathbf{k}} = C\{N\}, \quad (\text{A1})$$

$$\frac{\partial V'_{ZF}}{\partial t} = \frac{c^2}{B^2} \int d^2 k \frac{k_\theta k_r}{(1 + k_\theta^2 \rho_s^2)} N_k - \gamma_{damp} V'_{ZF}, \quad (\text{A2})$$

where γ_{damp} is ZF damping rate related to the collisionality and $C\{N\}$ accounts for local-in-scale interactions of turbulence.

Applying scale separation of wave action into mean value $\langle N_k \rangle$ and perturbation \tilde{N}_k , as $N_k = \langle N_k \rangle + \tilde{N}_k$, the drift wave group velocity $v_{gr} = \partial \omega_k / \partial k_r$, the shearing relation $\partial \omega_k / \partial x = k_\theta V'_{ZF}$, and a quasilinear approximation, we obtain an evolution of the mean population $\langle N_k \rangle$,

$$\frac{\partial \langle N_k \rangle}{\partial t} = \frac{\partial}{\partial k_r} D_k \frac{\partial \langle N_k \rangle}{\partial k_r}, \quad (\text{A3})$$

whereas

$$D_k = \sum_{q_r} q_r^2 k_\theta^2 |V_{ZF, q_r, \Omega}|^2 \tau_{q_r, \Omega}. \quad (\text{A4})$$

Here, $\tau_{q_r, \Omega}$ is the autocorrelation time between drift wave group velocity and the ZF group wave packet, obtained from Doppler-shifted frequency dispersion $\Delta(kv - \omega_k)$, which is

$$1/\tau_{q_r, \Omega} = |\Delta(kv - \omega_k)| = |(v - v_{gr})\Delta k|. \quad (\text{A5})$$

Thus, for quasi-particles with drift wave phase velocity $v = \omega_k/k = v_{ph}$ resonating with group propagation of the ZF shearing $v_{gr} = \partial \Omega / \partial q_r = v_{ph}$, we obtain

$$\tau_{q_r, \Omega} = \left| \left(\frac{\partial \Omega}{\partial q_r} - v_{gr}(k) \right) \Delta q_r \right|^{-1}, \quad (\text{A6})$$

where Δq_r is the typical width of the envelope of the ZF and MF wave packet. Rewriting the mean turbulence energy as I , i.e., $I \equiv \langle \epsilon \rangle = \int dk \omega_k \langle N_k \rangle$, we find a temporal evolution equation for turbulence intensity with linear growth and non-linear damping as well as shearing effects as

$$\frac{\partial I}{\partial t} = \gamma_L I - \Delta \omega I^2 - \sum_{q_r, \Omega} \alpha_{q_r, \Omega} I V_{ZF, q_r, \Omega}^2, \quad (\text{A7})$$

where $\alpha_{q_r, \Omega} \sim \tau_{q_r, \Omega}$ is the coupling parameter between turbulence and ZFs related to the correlation time of the shears.

Here, we retain two different modes of flows, i.e., meso-scale ZF and large scale mean flow. ZF has a shearing scale $q_r \sim 1/\sqrt{a\rho_i}$, while MF has $q_r \sim 1/L_n$, since MF shear is determined by the profile gradients. We finally obtain

$$\frac{\partial I}{\partial t} = \gamma_L I - \Delta \omega I^2 - \alpha_0 I E_0 - \alpha_V I E_V. \quad (\text{A8})$$

This comes to Eq. (1), including the additional nonlocal diffusion term.

Note that we neglect the geodesic curvature $-(2c_s/R) \langle (p_i + p_e) \sin \theta \rangle$ in the zonal flow evolution Eq. (A2). If the geodesic curvature includes, we may expect the higher frequency eigenmode of ZF, i.e., the geodesic acoustic mode (GAM). A model incorporating the geodesic curvature and also the sound wave propagation is discussed in Ref. 49. As most experimental results show, however, GAM is not relevant in I-phase and H-mode. Therefore, it is sufficient to neglect the geodesic curvature in the model incorporating the mean flow shearing. A screening factor of the zero-frequency ZF, $A_0 = (1 + 2q^2)^{-1}$, in the fluid closure may be included in the evolution of ZF, originating from the parallel nonlinearity. However, the screening factor does not qualitatively change the stability of the model. Thus, here we do not consider this additional effect, since we consider a minimal model of the feedback loop.

As the GAM in the I-phase is observed in ASDEX Upgrade,¹⁶ it is interesting to consider a turbulent state regulated by the GAM there. In the possible GAM and ZF coexisting state discussed in Ref. 49, we expect that no GAM will survive for lower q value. The GAM always suffers from higher damping than ZF. Thus, the GAM growth is weaker and drops with milder mean flow shearing interaction. Above a certain critical q , the GAM-only state can still be possible. In this self-regulation process, the energy input from turbulence to ZF drops considerably, while that from turbulence to the GAM persists. In such cases that the GAM is relevant, the turbulence spreading induced by the GAM may modulate the propagation speed of the LCO.²³ Furthermore, GAM and

ZF are more similar than different. Both are $n = 0$ (no transport) secondary modes excited by three wave interactions via modulational instability. Both shear the turbulence, and so extract energy from it. The major difference is that GAMs have $\omega \sim c_s/R$, while ZFs have $\omega \sim 0$. Also, GAM propagates radially. We rather consider the similar basic structure of two predator (GAM and MF or ZF and MF)-one prey (turbulence) systems. Very similar results can be expected, but we expect additional sensitivity of the collisionless damping to the power threshold.

APPENDIX B: THE DERIVATION OF THE INHIBITION OF ZONAL FLOW SHEARING BY MEAN FLOW SHEARING

We discuss how ZF shear shrinks in the presence of the MF shear, based on the wavekinetic treatment.^{13,48} Here, we define $\langle V_E \rangle$ as the mean $E \times B$ shear flow and V_{ZF} as zonal flows with the form of $\exp(iq_r x)$. In the presence of the mean flow shear, the linearized wave kinetic equation for the perturbation \tilde{N}_k and mean $\langle N_k \rangle$ are written as

$$\frac{\partial \tilde{N}_k}{\partial t} + iq_r v_{gr} \tilde{N}_k - k_\theta \langle V_E' \rangle \frac{\partial \tilde{N}_k}{\partial k_r} + \gamma \tilde{N}_k = k_\theta V_{ZF}' \frac{\partial \langle N_k \rangle}{\partial k_r}. \quad (\text{B1})$$

Here, the effect of a mean shear flow $\langle V_E \rangle$ on \tilde{N}_k is explicitly shown in the third term on the l.h.s. of Eq. (B1). We solve Eq. (B1) along a non perturbed orbit by introducing a total time derivative D_t as

$$D_t = \frac{\partial}{\partial t} - k_\theta \langle V_E' \rangle \frac{\partial}{\partial k_r}. \quad (\text{B2})$$

In this coordinate, the shearing effect by $\langle V_E' \rangle$ is explicitly reflected in the linear increase of k_r in time as

$$D_t k_r = -k_\theta \langle V_E' \rangle. \quad (\text{B3})$$

Equation (B1) can be integrated along this nonperturbed orbit as

$$\tilde{N}_k(q_r, t) = \int_{-\infty}^t dt' \exp \left\{ -\gamma(t-t') - iq_r \int_{t'}^t dt'' v_{gr}(t'') \right\} \times k_\theta V_{ZF}'(p, t') \frac{\partial \langle N_k(t') \rangle}{\partial k_r(t')}, \quad (\text{B4})$$

where a term depending on the initial condition is dropped. The shearing effect by a mean flow is embedded in the time dependent group velocity v_{gr} and equilibrium wave quanta density spectrum $\partial \langle N_k(k_r(t')) \rangle / \partial k_r(t')$. In the limit where the mean shearing occurs on a time scale larger than other dynamical time scales (i.e., $1/\gamma$, $1/v_{gr} q_r$, and $1/\Omega$), we can approximate $\partial \langle N_k(k_r(t')) \rangle / \partial k_r(t') \sim \partial \langle N_k(k_r(t)) \rangle / \partial k_r(t)$. Note that if we take $v_{gr}(t'')$ and $k_r(t')$ to be constant, the result is the usual modulational instability without the mean flow shear. However, by taking into account the dependence of v_{gr} on $\langle V_E' \rangle$ through k_r , we expect the slowdown of the propagation of drift waves due to enhanced inertia via mean shearing. Then, the substitution of the time dependence of $\exp\{-i\Omega t\}$ for \tilde{N}_k and V_{ZF} simplifies Eq. (B4) to

$$\tilde{N}_k(q_r, \Omega) \sim k_\theta V_{ZF}' R \frac{\partial \langle N_k \rangle}{\partial k_r}. \quad (\text{B5})$$

Here, the real part of R becomes

$$\text{Re}(R) \sim \frac{1}{\gamma} \left[1 - \frac{12q_r^2 \langle V_E' \rangle^2 \omega_*^2 k_\theta^2}{\gamma^4} \right] \quad (\text{B6})$$

for $k_\perp \rho_s < 1$ and $\gamma > qv_{gr} > \Omega$, where $\omega_* = k_\theta v_* = k_\theta cT_e / eB_0 L_n$ is the electron diamagnetic drift frequency, originating from the group velocity. The sign of $\text{Re}(R)$ is always positive since R was obtained by treating the effect of $\langle V_E' \rangle$ as a small perturbation. From Eqs. (A2) and (B6), ZF growth is also obtained as

$$\Omega \sim iq_r^2 \int d^2 k \frac{k_\theta^2 k_r}{(1+k^2)^2} R \left(-\frac{\partial \langle N_k \rangle}{\partial k_r} \right). \quad (\text{B7})$$

From Eq. (B7), it is clearly shown that a mean flow shear *suppresses* the growth rate of zonal flows. The reduction arises due to the time variation of v_{gr} , related to the decorrelation of drift wave propagation by a shear flow, weakening the coherent modulation response of the drift wave spectrum. Thus, this effect is put as ζ_0 in Eq. (2).

- ¹F. Wagner, G. Becker, K. Behringer, D. Campbell, A. Eberhagen, W. Engelhardt, G. Fussmann, O. Gehre, J. Gernhardt, G. V. Gierke, G. Haas, M. Huang, F. Karger, M. Keilhacker, O. Klüber, M. Kornherr, K. Lackner, G. Lisitano, G. G. Lister, H. M. Mayer, D. Meisel, E. R. Müller, H. Murmann, H. Niedermeyer, W. Poschenrieder, H. Rapp, H. Röhr, F. Schneider, G. Siller, E. Speth, A. Stäbler, K. H. Steuer, G. Venus, O. Vollmer, and Z. Yü, *Phys. Rev. Lett.* **49**, 1408 (1982).
- ²Y. R. Martin, T. Takizuka, and ITPA CDBM H-Mode Threshold Database Working Group, *J. Phys.: Conf. Ser.* **123**, 012033 (2008).
- ³F. Ryter, T. Pütterich, M. Reich, A. Scarabosio, E. Wolfrum, R. Fischer, M. G. Adamov, N. Hicks, B. Kurzan, C. Maggi, R. Neu, V. Rohde, G. Tardini, and ASDEX Upgrade Team, *Nucl. Fusion* **49**, 062003 (2009).
- ⁴H. Zohm, *Phys. Rev. Lett.* **72**, 222 (1994).
- ⁵J. Cordey, D. Muir, V. Parail, G. Vayakis, S. Ali-Arshad, D. Bartlett, D. Campbell, A. Colton, A. Costley, R. Gill, A. Loarte, S. Neudachin, L. Porte, A. Sips, E. Springmann, P. Stubberfield, A. Taroni, K. Thomsen, and M. V. Hellermann, *Nucl. Fusion* **35**, 505 (1995).
- ⁶R. Colchin, B. Carreras, R. Maingi, L. Baylor, T. Jernigan, M. Schaffer, T. Carlstrom, N. Brooks, C. Greenfield, P. Gohil, G. McKee, D. Rudakov, T. Rhodes, E. Doyle, M. Austin, and J. Watkins, *Nucl. Fusion* **42**, 1134 (2002).
- ⁷P. H. Diamond, S.-I. Itoh, K. Itoh, and T. S. Hahm, *Plasma Phys. Controlled Fusion* **47**, R35 (2005).
- ⁸S. Champeaux and P. Diamond, *Phys. Lett. A* **288**, 214 (2001).
- ⁹H. Biglari, P. H. Diamond, and P. W. Terry, *Phys. Fluids B* **2**, 1 (1990).
- ¹⁰T. S. Hahm and K. H. Burrell, *Phys. Plasmas* **2**, 1648 (1995).
- ¹¹P. H. Diamond, Y. M. Liang, B. A. Carreras, and P. W. Terry, *Phys. Rev. Lett.* **72**, 2565 (1994).
- ¹²A. I. Smolyakov, P. H. Diamond, and M. Malkov, *Phys. Rev. Lett.* **84**, 491 (2000).
- ¹³E.-J. Kim and P. H. Diamond, *Phys. Rev. Lett.* **90**, 185006 (2003).
- ¹⁴T. Estrada, T. Happel, C. Hidalgo, E. Ascasibar, and E. Blanco, *EPL* **92**, 35001 (2010).
- ¹⁵S. J. Zweben, R. J. Maqueda, R. Hager, K. Hallatschek, S. M. Kaye, T. Munst, F. M. Poli, A. L. Roquemore, Y. Sechrest, and D. P. Stotler, *Phys. Plasmas* **17**, 102502 (2010).
- ¹⁶G. D. Conway, C. Angioni, F. Ryter, P. Sauter, and J. Vicente (ASDEX Upgrade Team), *Phys. Rev. Lett.* **106**, 065001 (2011).
- ¹⁷L. Schmitz, L. Zeng, T. L. Rhodes, J. C. Hillesheim, E. J. Doyle, R. J. Groebner, W. A. Peebles, K. H. Burrell, and G. Wang, *Phys. Rev. Lett.* **108**, 155002 (2012).

- ¹⁸G. S. Xu, B. N. Wan, H. Q. Wang, H. Y. Guo, H. L. Zhao, A. D. Liu, V. Naulin, P. H. Diamond, G. R. Tynan, M. Xu, R. Chen, M. Jiang, P. Liu, N. Yan, W. Zhang, L. Wang, S. C. Liu, and S. Y. Ding, *Phys. Rev. Lett.* **107**, 125001 (2011).
- ¹⁹M. A. Malkov and P. H. Diamond, *Phys. Plasmas* **16**, 012504 (2009).
- ²⁰T. Estrada, C. Hidalgo, T. Happel, and P. H. Diamond, *Phys. Rev. Lett.* **107**, 245004 (2011).
- ²¹T. S. Hahm, P. H. Diamond, Z. Lin *et al.*, *Plasma Phys. Controlled Fusion* **46**, A323 (2004).
- ²²B. A. Carreras, P. H. Diamond, and G. Vetoulis, *Phys. Plasmas* **3**, 4106 (1996).
- ²³K. Miki and P. H. Diamond, *Phys. Plasmas* **17**, 032309 (2010).
- ²⁴Z. H. Wang, P. H. Diamond, O. D. Gurcan, X. Garbet, and X. G. Wang, *Nucl. Fusion* **51**, 073009 (2011).
- ²⁵Z. Lin, T. S. Hahm, W. W. Lee, W. M. Tang, and P. H. Diamond, *Phys. Rev. Lett.* **83**, 3645 (1999).
- ²⁶F. L. Hinton, *Phys. Fluids B* **3**, 696 (1991).
- ²⁷X. Garbet, L. Garzotti, P. Mantica, H. Nordman, M. Valovic, H. Weisen, and C. Angioni, *Phys. Rev. Lett.* **91**, 035001 (2003).
- ²⁸M. B. Isichenko, A. V. Gruzinov, and P. H. Diamond, *Phys. Rev. Lett.* **74**, 4436 (1995).
- ²⁹B. Coppi and C. Spight, *Phys. Rev. Lett.* **41**, 551 (1978).
- ³⁰W. M. Tang, G. Rewoldt, and L. Chen, *Phys. Fluids* **29**, 3715 (1986).
- ³¹S. H. Müller, J. A. Boedo, K. H. Burrell, J. S. deGrassie, R. A. Moyer, D. L. Rudakov, and W. M. Solomon, *Phys. Rev. Lett.* **106**, 115001 (2011).
- ³²C. J. McDevitt, P. H. Diamond, O. D. Gurcan, and T. S. Hahm, *Phys. Plasmas* **17**, 112509 (2010).
- ³³S. P. Hirshman and D. J. Sigmar, *Nucl. Fusion* **21**, 1079 (1981).
- ³⁴J. B. Taylor, J. W. Connor, and P. Helander, *Phys. Plasmas* **5**, 3065 (1998).
- ³⁵M. A. Malkov and P. H. Diamond, *Phys. Plasmas* **15**, 122301 (2008).
- ³⁶S. Kim, H. Jhang, P. Diamond, L. Terzolo, S. Yi, and T. Hahm, *Nucl. Fusion* **51**, 073021 (2011).
- ³⁷K. Miyamoto, *Fundamentals of Plasma Physics and Controlled Fusion* (Iwanami, 1997).
- ³⁸C. Birdsall and A. Langdon, *Plasma Physics via Computer Simulation*, 1st ed., Series in Plasma Physics (Taylor & Francis, 2004).
- ³⁹R. W. Hamming, *Digital Filters (Dover Civil and Mechanical Engineering)*, 3rd ed. (Dover, 1997).
- ⁴⁰V. B. Lebedev and P. H. Diamond, *Phys. Plasmas* **4**, 1087 (1997).
- ⁴¹P. Manz, G. S. Xu, B. N. Wan, H. Q. Wang, H. Y. Guo, I. Cziegler, N. Fedorczak, C. Holland, S. H. Müller, S. C. Thakur, M. Xu, K. Miki, P. H. Diamond, and G. R. Tynan, *Phys. Plasmas* **19**, 072311 (2012).
- ⁴²T. Estrada, T. Happel, L. Eliseev, D. López-Bruna, E. Ascasíbar, E. Blanco, L. Cupido, J. M. Fontdecaba, C. Hidalgo, R. Jiménez-Gómez, L. Krupnik, M. Liniers, M. E. Manso, K. J. McCarthy, F. Medina, A. Melnikov, B. van Milligen, M. A. Ochando, I. Pastor, M. A. Pedrosa, F. L. Tabarés, D. Tafalla, and TJ-II Team, *Plasma Phys. Controlled Fusion* **51**, 124015 (2009).
- ⁴³J. Lang *et al.*, in US Transport Task Force Workshop, Anapolis, 2012.
- ⁴⁴N. Fedorczak, P. H. Diamond, G. Tynan, and P. Manz, *Nucl. Fusion* **52**, 103013 (2012).
- ⁴⁵W. Fundamenski, F. Militello, D. Moulton, and D. McDonald, *Nucl. Fusion* **52**, 062003 (2012).
- ⁴⁶Y. Xu, D. Carralero, C. Hidalgo, S. Jachmich, P. Manz, E. Martines, B. van Milligen, M. A. Pedrosa, M. Ramisch, I. Shesterikov, C. Silva, M. Spolaore, U. Stroth, and N. Vianello, *Nucl. Fusion* **51**, 063020 (2011).
- ⁴⁷D. E. Newman, B. A. Carreras, D. Lopez-Bruna, P. H. Diamond, and V. B. Lebedev, *Phys. Plasmas* **5**, 938 (1998).
- ⁴⁸P. H. Diamond, S.-I. Itoh, and K. Itoh, *Modern Plasma Physics: Volume 1, Physical Kinetics of Turbulent Plasmas*, 1st ed. (Cambridge University Press, 2010).
- ⁴⁹K. Miki and P. H. Diamond, *Nucl. Fusion* **51**, 103003 (2011).